*Burns & Trauma*, 2024, **12**, 1–19
https://doi.org/10.1093/burnst/tkae035
**Research Article**

# Neuregulin-1, a member of the epidermal growth factor family, mitigates STING-mediated pyroptosis and necroptosis in ischaemic flaps

**Xuwei Zhu[1,2,3,‡], Gaoxiang Yu[1,2,3,‡], Ya Lv[4,‡], Ningning Yang[1,2,3], Yinuo Zhao[5], Feida Li[1,2,3], Jiayi Zhao[3], Zhuliu Chen[1,2,3], Yingying Lai[1,2,3], Liang Chen[1,2,3], Xiangyang Wang[1,2,3], Jian Xiao[6], Yuepiao Cai[6], Yongzeng Feng, Jian Ding[1,2,3,*], Weiyang Gao[1,2,3,*], Kailiang Zhou[1,2,3,*], Hui Xu[1,2,3,*]**

[1]Department of Orthopaedics, The Second Affiliated Hospital and Yuying Children's Hospital of Wenzhou Medical University, No. 109 West Xueyuan Road, Lucheng District, Wenzhou 325027, China
[2]Zhejiang Provincial Key Laboratory of Orthopaedics, No. 109 West Xueyuan Road, Lucheng District, Wenzhou 325027, China
[3]The Second Clinical Medical College of Wenzhou Medical University, No. 109 West Xueyuan Road, Lucheng District, Wenzhou 325027, China
[4]The First Affiliated Hospital of Wenzhou Medical University, Nanbaixiang Street, Ouhai District, Wenzhou 325000, China
[5]School of Pharmaceutical Science of Zhejiang Chinese Medical University, NO. 548 Binwen Road, Binjiang District, Hangzhou 310000, China
[6]Molecular Pharmacology Research Center, School of Pharmaceutical Science, Wenzhou Medical University, Chashan University Town, Ouhai District, Wenzhou, 325000, China

*Correspondence. Jian Ding, Email: dingdingdang9770@163.com; Weiyang Gao, Email: weiyanggaoi@126.com; Kailiang Zhou, Email: zhoukailiang@wmu.edu.cn; Hui Xu, Email:13968800082@163.com

‡These co-first authors contributed equally to this work.

## Abstract

**Background:** Ensuring the survival of the distal end of a random flap during hypoperfusion (ischaemia) is difficult in clinical practice. Effective prevention of programmed cell death is a potential strategy for inhibiting ischaemic flap necrosis. The activation of stimulator of interferon genes (STING) pathway promotes inflammation and leads to cell death. The epidermal growth factor family member neuregulin-1 (NRG1) reduces cell death by activating the protein kinase B (AKT) signalling pathway. Moreover, AKT signalling negatively regulates STING activity. We aimed to verify the efficacy of NRG1 injection in protecting against flap necrosis. Additionally, we investigated whether NRG1 effectively enhances ischemic flap survival by inhibiting pyroptosis and necroptosis through STING suppression.
**Methods:** A random-pattern skin flap model was generated on the backs of C57BL/6 mice. The skin flap survival area was determined. The blood supply and vascular network of the flap was assessed by laser Doppler blood flow analysis. Cluster of differentiation 34 immunohistochemistry (IHC) and haematoxylin and eosin (H&E) staining of the flap sections revealed microvessels. Transcriptome sequencing analysis revealed the mechanism by which NRG1 promotes the survival of ischaemic flaps. The levels of angiogenesis, oxidative stress, necroptosis, pyroptosis and indicators associated with signalling pathways in flaps were examined by IHC, immunofluorescence and Western blotting. Packaging adeno-associated virus (AAV) was used to activate STING in flaps.
**Results:** NRG1 promoted the survival of ischaemic flaps. An increased subcutaneous vascular network and neovascularization were found in ischaemic flaps after the application of NRG1. Transcriptomic gene ontology enrichment analysis and protein level detection indicated that necroptosis, pyroptosis and STING activity were reduced in the NRG1 group. The phosphorylation of AKT and forkhead box O3a (FOXO3a) were increased after NRG1 treatment. The increased expression of STING in flaps induced by AAV reversed the therapeutic effect of NRG1. The ability of NRG1 to phosphorylate AKT-FOXO3a, inhibit STING and promote flap survival was abolished after the application of the AKT inhibitor MK2206.
**Conclusions:** NRG1 inhibits pyroptosis and necroptosis by activating the AKT-FOXO3a signalling pathway to suppress STING activation and promote ischaemic flap survival.

**Keywords:** Neuregulin-1; STING; Pyroptosis; Necroptosis; Ischaemic flaps; Epidermal growth factor

### Highlights

- NRG1 promotes ischaemic flap survival by reducing pyroptosis and necroptosis through the inhibition of STING activity.
- NRG1 inhibits STING activation by activating the AKT-FOXO3a pathway to promote flap survival in ischaemic flaps.
- NRG1 is a potential therapeutic agent for ischaemic flaps.

## Background

There are two types of surgery in trauma and plastic reconstruction: excision and reconstruction [1]. Excision surgery, such as scar resection surgery, mainly involves the removal of abnormal proliferative tissues in the body. In contrast, reconstruction surgery is primarily aimed at restoring deficient functions through tissue transplantation, such as reconstructing skin barrier function through skin grafting. An important technique in reconstructive surgery is flap transplantation [2]. The survival of the skin flap is mediated by the joint action of the subdermal vascular

**Received:** November 15, 2023. **Revised:** May 22, 2024. **Accepted:** May 22, 2024

network and the vessels from the bed. Since flap transfer cuts off most of the blood supply to the flap, reconstruction of the capillaries distal to the flap often takes 5 to 10 days [3]. During this period, the distal terminal of the flap suffers from chronic ischaemia, which leads to an increased level of oxidative stress in the flap tissue [4]. Moreover, due to ischaemia, some cells inside the flap undergo necrosis and lysis, leading to the secretion of multiple inflammatory factors that exacerbate tissue injury and further affect flap survival [5]. If the viability of random skin flaps could be increased to inhibit ischaemic necrosis in the distal region and allow flap survival at the same low perfusion level as the skin graft, the various types of cell death of flaps at the molecular level could be inhibited, thus breaking the vicious cycle of ischaemia–oxidative stress–necrosis–inflammation–exacerbation of ischaemia–exacerbation of necrosis. This approach may increase the clinical applications of random skin flaps.

Cell death is a basic biological phenomenon in all organisms and is involved in functions such as embryonic development, organ maintenance and senescence through the coordination of the immune response and self-immunity [6]. Recently, with the in-depth study of programmed cell death (PCD), an increasing number of studies have confirmed the role of two types of PCD in ischaemic diseases and ischaemia–reperfusion injury [7,8]. Pyroptosis is caused by the activation of intracellular sensors such as nucleotide-binding domain leucine-rich-containing family pyrin domain-containing-3 (NLRP3) by external stimuli [reactive oxygen species, lipopolysaccharide and damage-associated molecular patterns (DAMPs)], which recruit the adaptor apoptosis-associated speck-like protein containing a caspase-recruitment domain (ASC), induce the formation of inflammasomes and activate caspase1, which in turn activates gasdermin D (GSDMD) and forms pores in the cell plasma membrane, leading to cell membrane collapse and triggering cell death and inflammatory mediator [interleukin (IL)-1$\beta$ and IL-18] release [9,10]. Necroptosis is activated after stimulation by the accumulation of receptor-interacting protein kinases (RIPKs), such as RIPK1 and RIPK3, which form necrosomes by phosphorylation [11]. In the absence of caspase8 activity, RIPK1 recruits and phosphorylates RIPK3, forming a complex called the ripoptosome [12]. Mixed lineage kinase domain-like protein (MLKL) is subsequently recruited by the ripoptosome and phosphorylated. MLKL translocates to the membrane and promotes membrane permeability, leading to necrosis [11,13]. According to previous studies and the results of transcriptome sequencing of mouse skin flaps, pyroptosis and necroptosis are identified as the two important forms of cell death resulting in skin flap necrosis [12,14]. Therefore, effectively preventing these two kinds of programmed death is likely to be an effective approach for inhibiting flap necrosis.

Regarding uncontrollable PCD and autoimmune inflammatory damage, another set of proteins that have been studied extensively recently are interferon gene-stimulating proteins [stimulator of interferon genes (STING), transmembrane protein 173 (TMEM173) and mediator of IRF3 activation (MITA)] [15]. STING has been revealed to be associated with the TMEM173-encoded ER, which detects abnormal DNA species in the cell cytoplasm and induces the secretion of multiple proinflammatory cytokines as well as type I interferon (IFN) [16]. STING activation is one of the key factors in uncontrolled sepsis and inflammation [17]. Recently, STING-mediated inflammation, the type I IFN response and cell death (such as apoptosis, pyroptosis and necroptosis) were shown to likely lead to sepsis or septic shock [17]. Abnormal activation of STING might lead to uncontrolled inflammation or even cell death [18]. The vicious cycle of ischemia, necrosis and inflammation exacerbating flap necrosis is akin to the uncontrolled inflammatory necrosis induced by STING. However, no study has yet examined the STING pathway in conjunction with flap necrosis. It remains unclear whether the STING pathway is involved in the inflammatory programmed necrosis pathway that results in uncontrollable pyroptosis and necroptosis in the ischaemic flap, and whether a breakthrough could be achieved to further research on suppressing flap necrosis.

Growth factor treatments offer benefits such as promoting tissue repair and regeneration, expediting healing, improving treatment outcomes and enabling personalized therapy [19,20]. Neuregulin-1 (NRG1) is an epidermal growth factor-like protein primarily found in the nervous and cardiovascular systems and is considered a key driver of tissue regeneration in multiple organs [21]. In hind-limb ischaemia models, NRG1 has been identified as a crucial mediator of angiogenesis [20], while its activation during myocardial injury protects against microvascular endothelial damage and reduces oxidative stress and cell death [22,23]. Additionally, this molecule is involved in suppressing immune inflammation during septic cardiomyopathy [21]. NRG1 has been shown to stimulate intestinal crypt proliferation and induce organoid budding via the mitogen-activated protein kinase and protein kinase B (PKB/AKT) pathways [24]. A recent study has revealed that NRG1 regulates the growth and migration of fibroblasts and keratinocytes through the extracellular signal-regulated kinase pathway, thereby promoting wound healing [25]. As a multifunctional endogenous protein that inhibits inflammatory responses, promotes angiogenesis, facilitates tissue repair and regeneration, and suppresses cell death, NRG1 may be the optimal choice for increasing the survival of ischaemic regions in skin flaps. Moreover, AKT kinase plays a negative regulatory role in antiviral immune responses mediated by cyclic GMP-AMP synthase (cGAS)-STING [26]. Therefore, we hypothesized that the suppressive effects of NRG1 on cell death and oxidative stress are associated with STING inhibition. In addition, the role of NRG1 in skin flap tissue has never been studied. We also speculated that NRG1 could improve the survival of ischaemic flaps by modulating STING and PCD, and further explored the underlying mechanism involved.

## Methods

### Animals

Healthy C57BL/6 mice (adult males, 20–30 g) were provided by the Experimental Animal Center of Wenzhou Medical University (SCXK [ZJ] 2015–0001). The animal experiments performed in this study conformed to the Guidelines for the Welfare and Usage of Laboratory Animals of the China National Institutes of Health and were approved by the Animal Welfare and Use Committee of Wenzhou Medical University (wydw2024–0058). Animals were fed under standard conditions (temperature: 21–25°C, humidity: 50–60%, light/dark cycle: 12/12 h) and allowed to drink and eat freely. The surgery, treatment and perioperative nursing of the

experimental animals were conducted according to the Guidelines for the Care and Use of Experimental Animals of The Chinese Academy of Health.

## Random-pattern skin flap modelling

According to previous studies, mice were anaesthetized with 1% pentobarbital sodium (50 mg/kg) via intraperitoneal injection [12,14]. All hair on the back of the mice, from below the ears to the base of the tail, was then removed. The dorsal flap was designed with the bilateral posterior superior iliac spine as the base (size: $1.5 \times 4.5$ $cm^2$). The root and all visible vessels around the flap were removed and only the skin was connected. Finally, the edges of the flap were gently sutured with a 4–0 nonabsorbable line. The random flaps were grouped into proximal (zone-I), middle (zone-II) and distal (zone-III) groups, each of which was of equal size. The division of the mouse dorsal skin flap into three distinct areas was guided by the modified McFarlane flap model and previous studies [27–29]. Zone-I represents healthy tissue, zone-III is predisposed to necrosis without intervention and zone-II serves as the pivotal intermediate zone prone to ischaemia and subsequent necrosis. Focusing therapeutic interventions on zone-II, the watershed region, allows us to mitigate ischaemia and forestall necrosis, which is considered a crucial part of increasing flap survival. Therefore, zone-II was the focal point of histological and molecular biological evaluations. All mice were sacrificed on 7 days after the operation for the next step of the experiment.

## Adeno-associated virus vector packaging

pAV-U6-STING-CGA-EGFP was generated by synthesizing a Sting1 sequence and cloning it into the pAV-U6-MCS-CGA-EGFP (GV478) plasmid. Subsequently, the pAV-U6-STING-CGA-EGFP, Ad helper (adenovirus helper plasmid), and Adeno-associated virus (AAV) Rep/Cap expression plasmids were utilized to generate AAV9-U6-STING-CGV-EGFP by transfecting AAV-293 cells. Similarly, a scramble control was generated via AAV9-U6-scramble-CGV-EGFP. An iodixanol gradient approach was used to purify the viral particles.

## Drugs and AAV vector administration

For the determination of the optimal therapeutic drug concentration, 30 C57BL/6 mice were randomly assigned to the NRG1 (0, 1, 5, 15, 30 or 50 $\mu$g/kg/d) group, with 5 mice in each group. For the analysis of changes in endogenous NRG1 at different time points, 12 C57BL/6 mice were randomly assigned to four groups: days 0, 1, 3 and 7, with 3 mice in each group. A total of 150 C57BL/6 mice were randomly divided into 7 groups: control group (n = 35), NRG1 group (n = 35), AAV-STING group (n = 20), NRG1 + AAV-scramble group (n = 20), NRG1 + AAV-STING group (n = 20), MK2206 group (n = 10) and NRG1 + MK2206 group (n = 10). Recombinant human NRG1-$\beta$1 was first reconstituted at a concentration of 100 $\mu$g/ml in sterile phosphate-buffered saline (PBS) containing 0.1% bovine serum albumin (BSA). At a dosage of 15 $\mu$g/kg/day, the protein was further diluted in 50 $\mu$l of sterile PBS for intraperitoneal injection 7 days after flap surgery for the NRG1 group [24,30], while the control group was treated with an equal volume of saline. The NRG1 + AAV-scramble group, AAV-STING group and NRG1 + AAV-STING group were intravenously injected with 100 $\mu$l of viral vector containing $2.5 \times 10^{10}$ packaged genomic viral particles in PBS 14 days prior to surgery. Fourteen days later, the NRG1 + AAV-scramble group, NRG1 + AAV-STING group and NRG1 group received the same treatment (flap surgery and NRG1 intraperitoneal injection for 7 days). MK2206 was orally administered to mice in the NRG1 + MK2206 and MK2206 groups at a dosage of 120 mg/kg three times a week for two consecutive weeks [31]. Following flap surgery, both the NRG1 + MK2206 and MK2206 groups received either NRG1 or an equivalent volume of saline for 7 days. All animals were sacrificed with excessive pentobarbital sodium 7 days after surgery and tissues were sampled.

## Reagents and antibodies

Hematoxylin and eosin (H&E) staining kit (Cat. No. G1120) was provided by Solarbio Science & Technology (Beijing, China). An enzyme-linked immunosorbent assay (ELISA) kit (Cat. No. EM1239) was purchased from FineTest (Wuhan, China). AAV-Sting1 AAV (serotype-9, GENE-ID: 72512, GenBank: NM-028261) was designed and provided by GeneChem Chemical Technology Co, Ltd (Shanghai, China). Recombinant human NRG1-$\beta$1 (Cat. No. 396-HB-50) was prepared by R&D Systems (MN, USA). MK2206 (Cat. No. HY-10358) was provided by MedChemExpress (NJ, USA). The protease inhibitor cocktail (Cat. No. P8340) and phosphatase inhibitor cocktail (Cat. No. P0044) were purchased from Sigma–Aldrich (MO, USA). Primary antibodies against NLRP3 (Cat. No. 15101), caspase8 (Cat. No. 4790), RIPK1 (Cat. No. 3493), phosphorylated RIPK1 (pRIPK1) (Cat. No. 44590), RIPK3 (Cat. No. 10188), pRIPK3 (Cat. No. 91702), AKT (Cat. No. 4691), pAKT (Cat. No. 4060), forkhead box O3a (FOXO3a) (Cat. No. 12829), pFOXO3a (Cat. No. 9464), $\beta$-actin (Cat. No. 8457), MLKL (Cat. No. 37705), cGAS (Cat. No. 79978), pSTING (Cat. No. 50907) and endothelial nitric oxide synthase (eNOS) (Cat. No. 9586) were all purchased from Cell Signaling Technology (CST, USA). Superoxide dismutase 1 (SOD1) (Cat. No. 10269–1-AP), heme oxygenase 1 (HO1) (Cat. No. 10701–1-AP), vascular endothelial growth factor (VEGF) (Cat. No. 19003–1-AP), matrix metalloproteinase 9 (MMP9) (Cat. No. 10375–2-AP), caspase1 (Cat. No. 22915–1-AP), GSDMD (Cat. No.66387–1-Ig), secondary antibodies goat anti-mouse IgG (H + L), goat anti-rabbit IgG (H + L), horseradish peroxidase (HRP) conjugate (Cat. No. SA00001–1) and HRP conjugate (Cat. No. SA00001–2) were obtained from Proteintech Group (PG, USA). GSDMD-N (Cat. No. DF13758) was purchased from Affinity Biosciences (Nanjing, China). pMLKL (Cat. No. ab196436), STING (Cat. No. ab239074), IL-18 (Cat. No. ab207323), goat anti-mouse IgG H&L (DyLight® 488) (Cat. No. ab96871), goat anti-rabbit IgG H&L (DyLight® 488) (Cat. No. ab96883), goat anti-mouse IgG H&L (DyLight® 594) (Cat. No. ab96873), goat anti-rabbit IgG H&L (DyLight® 594) (Cat. No. ab96885) and 4,6-diamino-2-phenyl indole (DAPI) mounting medium aqueous, Fluoroshield (Cat. No. ab104139) were all purchased from Abcam (Cambridge, UK). IL-1$\beta$ (Cat. No. A11369) and cadherin 5 (Cat. No. A0734) were obtained from ABclonal Technology (Boston, MA, USA). NE-PER™ nuclear and cytoplasmic extraction reagents (Cat. No. 78835) and a bicinchoninic acid (BCA) kit (Cat. No. 23227) were provided by Thermo Fisher Scientific (Rockford, IL, USA). The 10, 12.5 and 15% sodium dodecyl sulfate–polyacrylamide gel electrophoresis (SDS–PAGE) gels (Cat. No. PG112,113 114) and the enhanced chemiluminescence HRP kit (Cat. No. SQ101) were obtained from EpiZyme (Shanghai, China).

Skim milk (Cat. No. P0216), 4% paraformaldehyde (Cat. No. P0099) and goat serum (Cat. No.C0265) were provided by Beyotime (Shanghai, China).

### Calculation of the flap survival area

On days 1, 3 and 7, a SONY RX100 III camera was used to capture high-resolution images for evaluating flap survival. The images were then imported into ImageJ software (version 2.14, NIH, Germany) to quantify the flap viability area. The formula for calculation is as follows: proportion of flap living area = flap living area/total area $\times$ 100%.

### Laser Doppler blood flow analysis

The blood supply and vascular network of the flap were assessed using laser Doppler blood flow (LDBF) analysis. On postoperative days 1 and 7, anaesthetized mice were positioned prone and the dorsal region was scanned using a laser Doppler flow analyzer (Moor Instruments, Axminster, UK). The LDBF analysis data were quantified using moorLDI software (version 6.1). Perfusion units were calculated and each scan was repeated at least three times.

### H&E staining

On day 7 after surgery, mice were sacrificed and six tissue specimens ($1 \times 1$ cm) were extracted from zone-II of the flap. The samples were fixed with 4% paraformaldehyde and subsequently paraffin embedded. Tissue sections (4 $\mu$m thick) were prepared and subjected to H&E staining, with slides observed under a light microscope (200x, Olympus Corporation, Japan). The modulations of inflammatory infiltration and microvascular reconstruction were assessed through microscopic examination. The average vascular density of the flap was calculated by determining the number of vessels per unit area (/mm$^2$) in at least five randomly selected sections, providing an indication of microcirculation.

### Immunohistochemistry

After baking, the tissue sections were dewaxed in xylene, followed by rehydration in a gradient ethanol bath. For antigen repair, the sections were cleaned, blocked with 3% (v/v) $H_2O_2$, and boiled in sodium citrate solution (10.2 mM). After cooling, the slices were blocked using 10% goat serum, followed by incubation overnight with primary antibodies, including anti-cluster of differentiation (CD)34 (1 : 100) and anti-SOD1 (1 : 100), in a wet box at 4°C. After rewarming and washing, the samples were coincubated with an enzyme-conjugated secondary antibody, stained with 3,3′-diaminobenzidine DAB solution and counterstained with haematoxylin. Images were taken with a DP2-TWAIN Image Acquisition System (dual targeted intracellular activity sensor (DTIAS), 200x, Olympus fluorescence microscope, Japan) and subjected to ImageJ software analysis to quantify the densities of CD34$^+$ vessels and the overall absorbance of SOD1$^+$ tissues. All measurements were taken from at least five random regions selected from three independent random slices.

### Immunofluorescence

Similar to the immunohistochemical protocol, the sections were dewaxed, rehydrated, sealed with 3% $H_2O_2$ and boiled in sodium citrate (SC) buffer (10.2 mM) for antigen repair. Then, the sections were incubated with primary antibodies against caspase1 (1 : 100), GSDMD-N (1 : 200), RIPK3 (1 : 200), pMLKL (1 : 100), CD31 (1 : 200), STING (1 : 200) and FOXO3a (1 : 400) at 4°C overnight. After 24 h, the samples were coincubated at room temperature in the dark with secondary antibodies, followed by DAPI counterstaining. The specimens stained with caspase1, GSDMD-N, RIPK3, pMLKL and CD31 were imaged using a Zeiss LSM 800 confocal microscope (Carl Zeiss, Germany). Image acquisition and processing were performed using Zeiss Zen Blue software. Specimens stained with STING and FOXO3a were imaged using a DTIAS. All slice images were captured within the dermis of the skin; five random areas of three random slices from zone-II of the skin flaps of each animal were imaged. The fluorescence intensity of caspase1, GSDMD-N, RIPK3 and pMLKL in each endothelial cell marked by CD31 and the fluorescence intensity of STING-positive cells within the dermal layer of the skin were quantified using ImageJ. The percentage of FOXO3a nuclear-excluded cells was calculated.

### Western blotting

After the animals were sacrificed, tissue samples were collected from the same size area ($5 \times 5$ mm) in Zone II of the skin flaps of each group. After the tissue protein was extracted from the flap with lysis buffer containing protease inhibitor cocktail and phosphatase inhibitor cocktail, protein concentrations were determined with a Pierce BCA protein assay kit. Protein (30 $\mu$g) was electrophoresed on a 10–15% SDS–PAGE gel and then transferred to a polyvinylidene fluoride (PVDF) membrane. The membrane was then blocked with 5% (w/v) skim milk at room temperature followed by incubation overnight at 4°C with the following protein probes (all 1 : 1000): IL-1$\beta$, IL-18, ASC, NLRP3, caspase1, GSDMD, RIPK1, RIPK3, MLKL, pMLKL, casepase8, SOD1, HO1, eNOS, VEGF, cadherin5, MMP9, $\beta$-actin, AKT, STING, FOXO3a, pAKT, pFOXO3A, pSTING and cGAS. Finally, protein bands were visualized by an enhanced chemiluminescence HRP kit after incubation with the enzyme-conjugated IgG secondary antibody at room temperature for 2 h. The signals were analysed using a ChemiDicTM XRS plus imaging system (Bio-Rad, USA).

### RNA sequencing and differential gene expression analysis

Total RNA was extracted from the second region of the skin flap using TRIzol reagent. The RNA purity and quantity were determined with a NanoDrop 2000 spectrophotometer. The RNA integrity was verified using an Agilent 2100 biological analyser. A cDNA library was constructed with a TruSeq single-chain messenger RNA long transcript (mRNA LT) sample preparation kit. RNA sequencing and bioinformatics analysis were performed by OE Biotechnology. Library sequencing was conducted on an Illumina HiSeq-X Ten platform, generating 125/150 bp reads at both ends. After processing by Trimmomatic, clean reads were finally obtained by discarding reads harbouring poly-N or low-quality sequences and subsequently localized to the mouse genome using HISAT2 (GRCM38.p6). Cufflinks was used to analyse the count for each gene and HTSeq-count was applied to compute the number of read codes. The DESeq2 package was utilized for differentially expressed gene (DEG) analysis. A $p$ value $< 0.05$ combined with a fold-change of either $>2$ or $<0.5$ was set as the threshold for DEG identification. Hierarchical cluster analysis of DEGs was further conducted to reveal gene expression patterns in different experimental groups and samples. According to the hypergeometric distribution, Gene Ontology (GO) enrichment and Kyoto Encyclopedia of Genes

and Genomes (KEGG) analysis of DEGs was conducted using R software.

### ELISA

The flap tissues were homogenized in PBS and subjected to repeated freeze–thaw cycles in liquid nitrogen. The homogenate was centrifuged at 10,000 × g for 10 min at 4°C and the supernatant was collected for further analysis. The levels of NRG1 in the flaps were determined using the ELISA kit according to the manufacturer's instructions. The optical density was measured at a wavelength of 450 nm.

### Statistics

Statistical assays were completed via the SPSS 22 program (USA). Data normality was assessed with the Shapiro–Wilk test. Normally distributed data are expressed as the mean ± standard deviation (SD) and were analysed using independent-sample t tests or one-way analysis of variance (ANOVA) with appropriate *post hoc* tests. Non-normally distributed data are reported as medians with interquartile ranges and were analysed using Mann–Whitney U or Kruskal–Wallis tests, as applicable. A $p$ value $<0.05$ was considered to indicate statistical significance, ensuring the application of appropriate statistical methods based on the data distribution.

## Results

### NRG1 increased the survival of ischaemic flaps

After random skin flap surgery in mice, necrosis usually begins gradually on the third day, and the skin becomes dark, dry, shrunken and stiff (Fig. 1a). First, an ELISA was used to track alterations in the endogenous NRG1 levels in the skin flap after model establishment. The results indicated a gradual increase in endogenous NRG1 levels over time (0, 1 and 3 days), suggesting a potential association between NRG1 and ischaemic flap survival (Fig. S1a, see online supplementary material). Then, based on the concentrations of NRG1 utilized in previous research [24,30], various concentrations (0, 1, 5, 15, 30 and 50 $\mu$g/kg) were selected to assess the impact of NRG1 on ischaemic flaps. Mice treated with NRG1 (15 $\mu$g/kg/day) exhibited significantly higher survival rates compared to those treated with 0, 1 and 5 $\mu$g/kg/day, demonstrating statistical significance. Although the average survival rate in the 15 $\mu$g/kg/day group was higher than that in the 30 and 50 $\mu$g/kg/day groups, no statistical significance was observed. (Fig. S1b, c). Analysis of the LDBF signal revealed a consistent trend with the flap survival outcome, determining 15 $\mu$g/mg as the optimal therapeutic concentration (Fig. S1d, e). The survival areas of the mouse skin flaps were significantly greater in the NRG1 group than in the control group (Fig. 1a, b, e). LDBF analysis further revealed differences in the intensities of blood flow signals in the mouse flaps (Fig. 1c, d). The LDBF signal on the seventh postoperative day was much stronger in the NRG1 group than in the control group (Fig. 1f). H&E staining and examinations were performed on tissues in zone-II of the flaps (Fig. 1g). Compared to that in the control group, the degree of vascularization of the flap tissue in zone-II of the NRG1 group increased. As shown in the enlarged H&E images, fewer visible micro-vessels were observed in the dermal region of the skin flap in the control group, and the mean vessel density was significantly lower than that found in the NRG1 group (Fig. 1g, j). CD34 immunohistochemical staining was used to label the microvessels of the flap (Fig. 1h), and the numbers of microvessels were calculated by microscopic observation. Consistent with the H&E staining results, the numbers of microvessels in the NRG1 group was significantly promoted (Fig. 1k). The expression levels of the angiogenesis-related proteins (cadherin 5, VEGF and MMP9) were further assessed by western blotting. The results showed that protein expression was significantly upregulated in the NRG1 group (Fig. S2a, b, see online supplementary material). Oxidative stress is an important component of skin-flap ischaemic injury [32]. Therefore, SOD1, HO1 and eNOS, which have inhibitory effects on oxidative stress, were identified as key indicators of oxidative stress. As indicated in Fig. 1i, l, the SOD1 expression level was significantly increased in the NRG1 group, while Western blotting revealed that HO1, SOD1 and eNOS were upregulated in the NRG1 group (Fig. S2c, d), suggesting that NRG1 effectively inhibited oxidative stress caused by skin flap injury. These results revealed that NRG1 was beneficial for flap survival.

To further investigate the underlying mechanisms involved, we performed transcriptome sequencing of both the control and NRG1 groups. It was found that NRG1 administration induced 2162 gene expression changes (1275 gene candidates were upregulated and 887 were downregulated), as indicated in the heatmap (Fig. S2e). Principal component analysis revealed significant disparities in mRNA expression profiles between control and NRG1 groups, while samples within each group demonstrated reproducibility (Fig. S2f). In addition, GO analysis suggested that most of the DEGs were correlated with inflammatory responses, cell necroptosis and pyroptosis, as well as oxidative stress (Fig. 2a). According to the RNA-seq data, NRG1 promoted flap survival by potentially inhibiting cell death processes, such as cell pyroptosis and necroptosis.

### NRG1 inhibited pyroptosis in ischaemic flaps

Previous studies have revealed the role of pyroptosis in flap necrosis, as this process inhibits vascular regeneration and reduces the viability of the flap [33,34]. Transcriptome sequencing suggested that pyroptosis levels in the NRG1 group were much lower than those in the control group. Here, western blotting revealed that the expression levels of the pyroptosis-related proteins (cleaved-caspase1, ASC, NLRP3, GSDMD-N, IL-18 and IL-1$\beta$) were significantly decreased in the NRG1 group (Fig. 2b, c). In addition, immunofluorescence staining was used to determine whether this treatment reduced the expression levels of pyroptosis markers (caspase1 and GSDMD-N) in the $CD31^+$ endothelial cells of the flap (Fig. 2d, e). Quantitative analysis revealed that NRG1 substantially reduced the integrated intensity of both $GSDMD\text{-}N^+$ and $caspase1^+$ cells among the $CD31^+$ endothelial cells of the flap's dermal layer (Fig. 2f, h). These results indicated that NRG1 inhibited pyroptosis in ischaemic flaps.

### NRG1 inhibited necroptosis in ischaemic flaps

Necroptosis is another cell death form of ischaemic flap necrosis [35]. The RNA-seq results indicated that necroptosis in the NRG1 group was significantly lower than that in the control group. Therefore, the expression levels of the necroptosis-associated proteins were further determined by western blotting and immunofluorescence assays (Fig. 3a, b). Compared to the control group, the levels of RIPK1, RIPK3

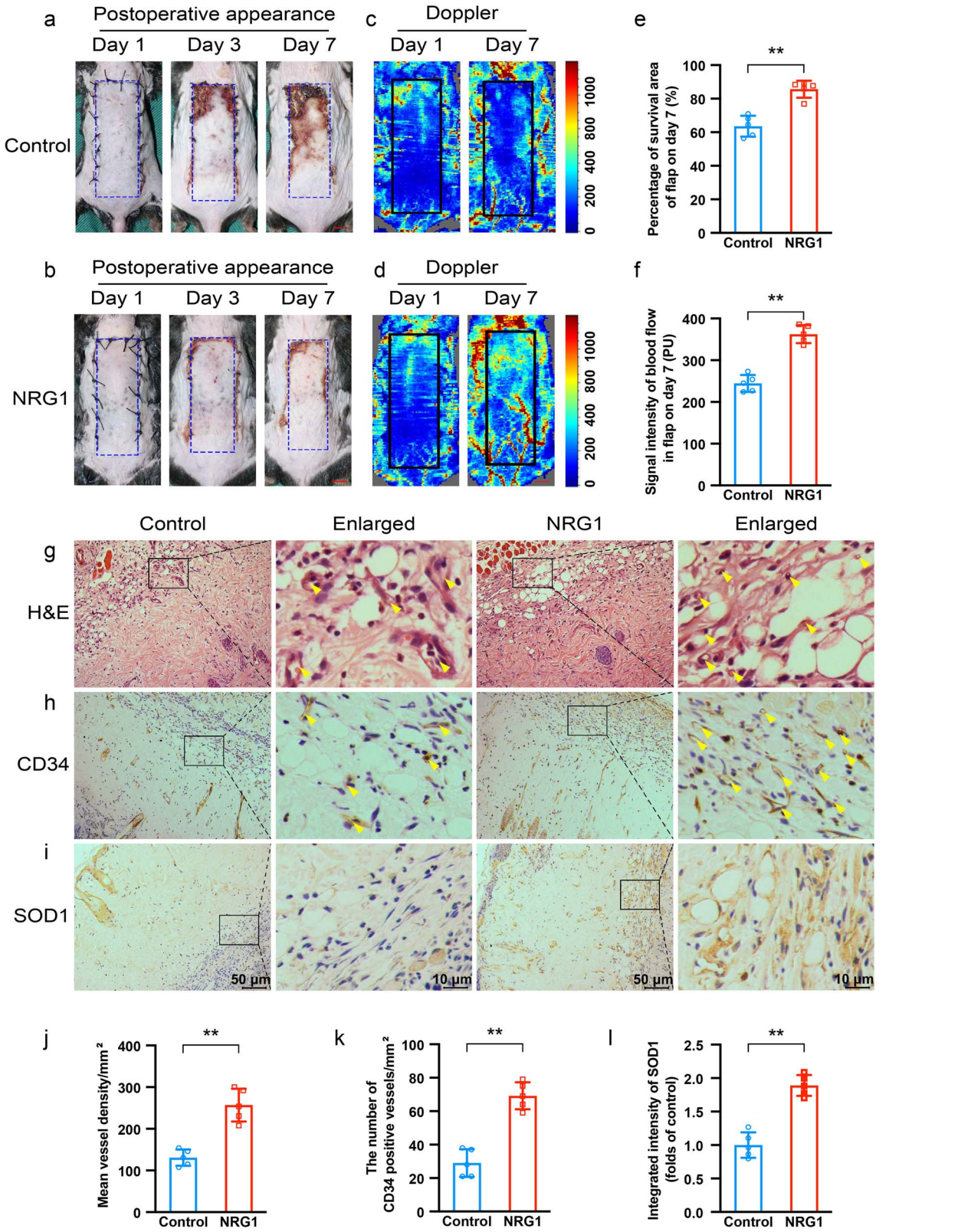


Figure 1. NRG1 increased the survival rate of ischaemic skin flaps. (**a**,**b**) Survial areas of control and NRG1 groups on days 1, 3 and 7 after surgery. (**c**,**d**) LDBF analysis on days 1 and 7. (**e**) Comparison of the percentage of survival area between two groups (n = 5). (**f**) Comparison of the LDBF analysis signals between two groups on day 7 (n = 5). (**g**) H&E staining of zone-II of the flaps in the two groups (scale bar = 50 $\mu$m, scale bar in the enlarged image = 10 $\mu$m). Yellow arrows indicate microvessels. (**h**) Immunohistochemical staining of CD34 (brown) in Zone-II of flaps in the two groups (scale bar = 50 $\mu$m, scale bar in the enlarged image = 10 $\mu$m). Yellow arrows indicate microvessels. (**i**) Immunohistochemical staining for SOD1 (brown) in zone-II of flaps in the two groups (scale bar = 50 $\mu$m, scale bar in the enlarged image = 10 $\mu$m). (**j**) Comparison of the vessel density (/mm $^2$) determined by H&E staining between two groups (n = 5). (**k**) Comparison of the number of CD34$^+$ vessels (/mm $^2$) between two groups (n = 5). (**l**) Comparison of the integrated intensity of SOD1 between two groups (n = 5). Two-tailed, unpaired t tests were conducted and the data are presented as the means ± SD, $^{**}p < 0.01$. *NRG1* neuregulin-1, *H&E* haematoxylin and eosin, *CD34* cluster of differentiation 34, *SOD1* superoxide dismutase 1

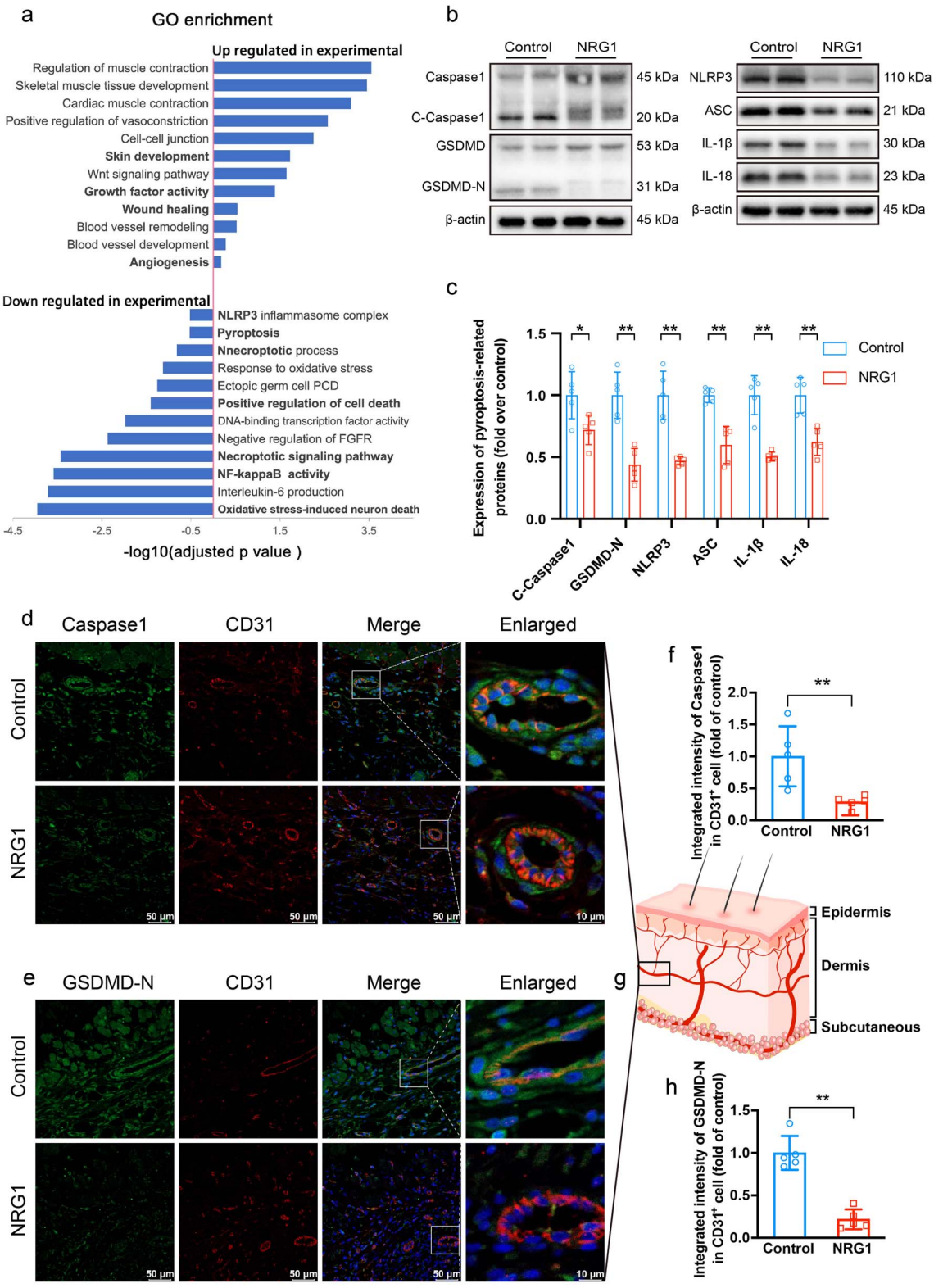


Figure 2. NRG1 inhibited cell pyroptosis in ischaemic flaps. (**a**) GO analysis of the target genes showing the biological processes influenced by NRG1 treatment. (**b**) Western blot results of caspase1, GSDMD, ASC, NLRP3, IL-18 and IL-1$\beta$ expression in control and NRG1 groups presented as typical images. $\beta$-Actin was utilized as a loading control. (**c**) Quantification of the protein levels of cleaved-caspase1, GSDMD-N, ASC, NLRP3, IL-18 and IL-1$\beta$ (n = 5). (**d**) Immunofluorescence staining of caspase1 (green), CD31 (red) and DAPI (blue) (scale bar = 50 $\mu$m, scale bar in the enlarged image = 10 $\mu$m). (**e**) Immunofluorescence staining of GSDMD-N (red), CD31 (green) and DAPI (blue) (scale bar = 50 $\mu$m, scale bar in the enlarged image = 10 $\mu$m). (**f**,**h**) Comparison of the integrated intensities of caspase1 and GSDMD-N in CD31$^+$ endothelial cells of the flap's dermal layer between two groups (n = 5). (**g**) Schematic diagram of the flap tissue, with the top representing the epidermis layer, the middle representing the dermis layer and the bottom representing the subcutaneous layer. The section is positioned in the dermis layer. Two-tailed, unpaired t tests were performed and the data are presented as the means ± SD, $^*p < 0.05$, $^{**}p < 0.01$. *NRG1* neuregulin1, *GO* gene ontology, *CD31* cluster of differentiation 31, *GSDMD* gasdermin D, *NLRP3* nucleotide-binding domain leucine-rich-containing family pyrin domain-containing-3, *ASC* adaptor apoptosis-associated speck-like protein containing a caspase-recruitment domain adaptor

and pMLKL were markedly lower in the NRG1 group, while the level of caspase8 was markedly greater. As shown in Fig. 3c–f, the fluorescence integrated intensities of RIPK3 and pMLKL in the $CD31^+$ endothelial cells of the flap's dermal layer in the NRG1 group were significantly lower than those in the control group. Overall, the protective effects of NRG1 on ischaemic flaps were found to be associated with inhibition of necroptosis.

## NRG1 inhibited STING activity in ischaemic flaps

Oxidative stress-induced DNA damage promotes activation of the cGAS-STING signalling pathway, which stimulates necroptosis and pyroptosis [36]. RNA-seq revealed a significantly lower Sting1 mRNA level in the NRG1 group (Fig. 3h), but whether the effect of NRG1 on pyroptosis and necroptosis is related to the cGAS-STING pathway is unclear. Key proteins of the cGAS-STING pathway were assessed. The western blotting outcomes showed that the expression levels of pSTING, STING and cGAS in the NRG1 group were downregulated (Fig. 3i, j). In addition, the immunofluorescence results demonstrated that the fluorescence integrated intensity of the STING-positive cells in the dermal layer of the flap was much lower in the NRG1 group than in the control group (Fig. 3k, l). In conclusion, these results confirmed that NRG1 decreased the activity of STING in ischaemic flaps.

## NRG1 reduced pyroptosis and necroptosis in ischaemic flap survival by inhibiting STING activity

To further confirm whether NRG1 inhibited pyroptosis and necroptosis in flaps by suppressing STING activity to promote flap survival, we overexpressed STING with AAV-STING. Five groups were used for comparison: the control group, the AAV-STING group, the NRG1 group, the NRG1 + AAV-scramble group and the NRG1 + AAV-STING group. Immunofluorescence and western blotting results (Fig. 4a–e) demonstrated that compared to those in the NRG1 and NRG1 + AAV-scramble groups, the STING level in the NRG1 + AAV-STING group was significantly greater. Compared to the control and NRG1 + AAV-STING groups, the AAV-STING group had a significantly greater STING level.

Subsequently, the potential therapeutic effects of NRG1 following AAV-STING transfection were assessed to further determine whether the inhibition of STING activity indeed increased flap survival. As shown in Fig. 5a, compared to those in the NRG1 and NRG1 + AAV-scramble groups, the flap survival areas in the NRG1 + AAV-STING group were significantly decreased. Additionally, the control and NRG1 + AAV-STING groups had a greater flap survival area than the AAV-STING group (Fig. 5a, e). The LDBF analysis results on day 7 showed that the blood flow signal intensities in the NRG1 + AAV-STING group were much lower than those in the NRG1 group and the NRG1+ AAV-scramble group, and those in the AAV-STING group were significantly lower than those in the NRG1 + AAV-STING group and the control group (Fig. 5b, f). Similarly, the gross results of H&E staining and flap survival were consistent. As indicated in Fig. 5c and the magnified H&E image in Fig. 5d, fewer visible microvessels were observed in the NRG1 + AAV-STING group, with a mean vessel density significantly lower than those found in the NRG1 and NRG1+ AAV-scramble groups; however, the mean vessel density in the AAV-STING group was much lower than that in the NRG1 + AAV-STING group and the control group. Finally, we further validated the levels of angiogenesis-related proteins (cadherin 5, VEGF and MMP9) and oxidative stress-related proteins (HO1, SOD1 and eNOS), demonstrating the same trend as previously described (Fig. S2g–j). These results indicated that NRG1 promoted the survival of ischaemic flaps by inhibiting STING activity.

The levels of pyroptosis and necroptosis were further investigated to determine whether the suppression of STING activity by NRG1 modulated PCD-related proteins. The results showed that the fluorescence integrated intensities of GSDMD-N and pMLKL in the $CD31^+$ endothelial cells of the flap's dermal layer were significantly greater in the NRG1 + AAV-STING group than in the NRG1 group and NRG1 + AAV-scramble group, while the fluorescence integrated intensities in the AAV-STING group were much greater than those in the NRG1 + AAV-STING group and the control group (Fig. 6a, b, e, f). In addition, the expression levels of pyroptosis-associated proteins (NLRP3, GSDMD-N, ASC, cleaved-caspase1, IL-18 and IL-1$\beta$) and necroptosis-associated proteins (RIPK1, RIPK3 and pMLKL) were significantly greater in the NRG1 + AAV-STING group than in the NRG1 group and NRG1 + AAV-scramble group, while the expression levels of these proteins in the AAV-STING group were greater than those in the AAV-STING group and the control group (Fig. 6c, d, g, h). These results suggested that the inhibition of STING activity after NRG1 treatment was an important mechanism by which NRG1 inhibited pyroptosis and necroptosis in ischaemic flaps and played a beneficial role.

## NRG1 activated the AKT-FOXO3a signalling pathway in ischaemic flaps

Many studies have proposed that the effects of NRG1 on tissue repair and anti-cell death are closely related to AKT activation [37,38]. Recent studies on STING have confirmed that AKT activation inhibits STING activity [26,39]. Thus, we hypothesized that the regulation of STING by NRG1 in ischaemic flaps might be related to its activation of AKT. As shown in Fig. 7a, KEGG enrichment revealed significant differences in the PI3K-AKT and FOXO signalling pathways between the NRG1 group and the control group. Further analysis of the expression levels of related proteins revealed that pAKT and pFOXO3a expression in the NRG1 group was significantly upregulated (Fig. 7b, c), suggesting that NRG1 activated the AKT-FOXO3a cell signalling pathway. To further determine whether the inhibition of STING after NRG1 treatment was regulated by the AKT–FOXO3a axis, we investigated the effects of the AKT-specific inhibitor MK2206 on the AKT–FOXO3a axis and ischaemic flap survival. The study was divided into four groups: the control group, the MK2206 group, the NRG1 group and the NRG1 + MK2206 group. The results shown in Fig. 7d, f revealed that the survival area of the flaps on the seventh day post-surgery was decreased in the NRG1 + MK2206 group compared to the NRG1 group. However, the survival area of the flaps in the NRG1 + MK2206 group was greater than that in the MK-2206 group. As depicted in Fig. 7e, g, the LDBF analysis results on the seventh day post-surgery showed that the blood flow signal intensity was lower in the NRG1 + MK2206 group compared to the NRG1 group, while the blood flow signal intensity in the MK-2206 group was lower than that in the NRG1 + MK2206 group. NRG1

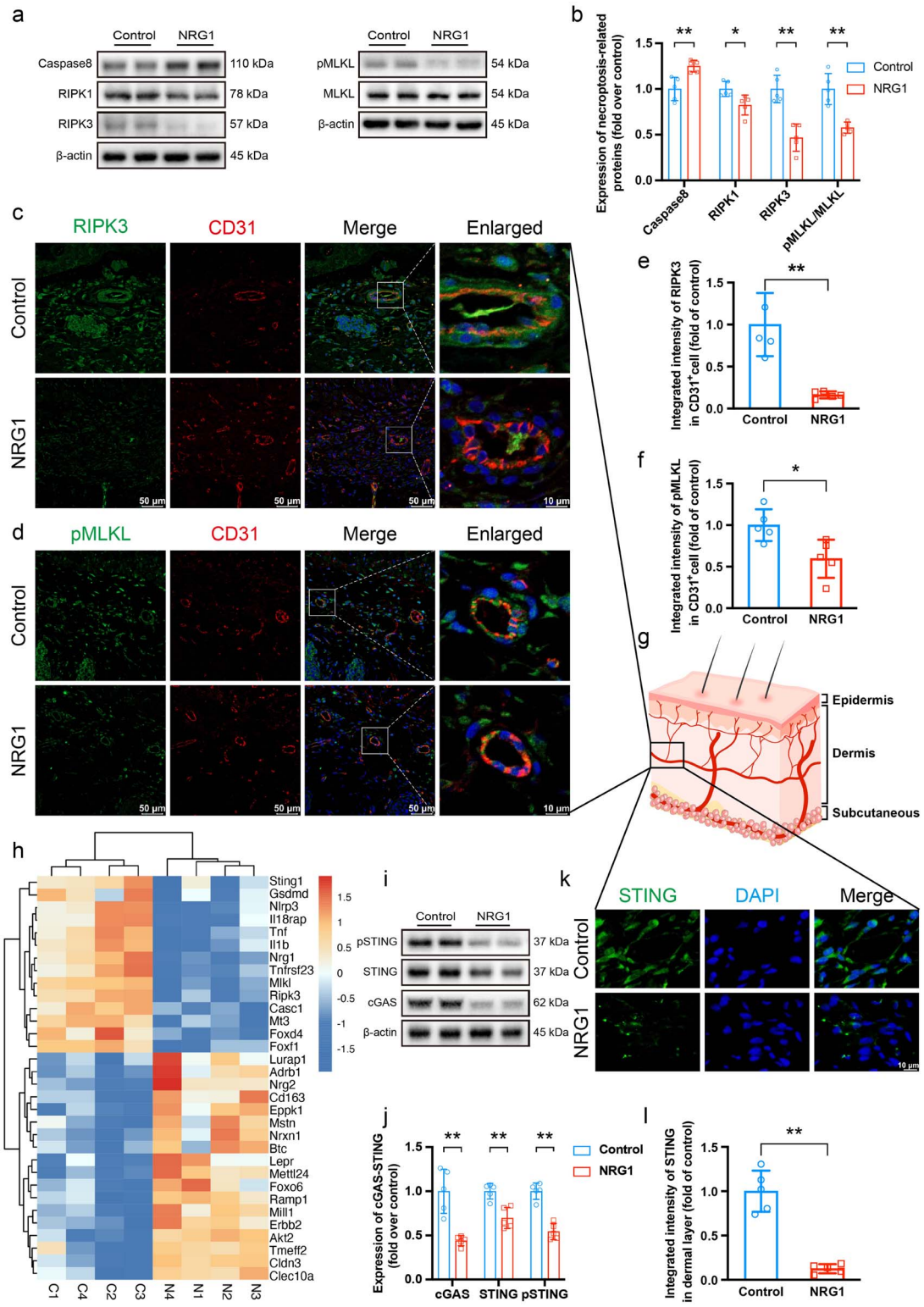


Figure 3. NRG1 inhibited cell necroptosis in ischaemic flaps. (**a**) Western blot results of RIPK1, RIPK3, MLKL, pMLKL and caspase8 expression in control and NRG1 groups presented as typical images. $\beta$-Actin was utilized as a loading control. (**b**) Quantification of the protein levels of RIPK1, RIPK3, pMLKL/MLKL and caspase8 (n = 5). (**c**) Immunofluorescence staining of RIPK3 (green), CD31 (red) and DAPI (blue) (scale bar = 50 $\mu$m, scale bar in the enlarged image = 10 $\mu$m). (**d**) Immunofluorescence staining of pMLKL (green), CD31 (red) and DAPI (blue) (scale bar = 50 $\mu$m, scale bar in the enlarged image = 10 $\mu$m). (**e**,**f**) Comparison of the integrated intensities of RIPK3 and pMLKL in CD31$^+$ endothelial cells of the flap's dermal layer between two groups (n = 5). (**g**) schematic diagram of the flap tissue; the section positioned in the dermis layer. (**h**) Heatmap of genes upregulated or downregulated by NRG1 injection in mouse skin tissue. (**i**) Western blot results of pSTING, STING and cGAS expression in control and NRG1 groups presented as typical images. $\beta$-Actin was utilized as a loading control. (**j**) Quantification of the protein levels of pSTING, STING and cGAS (n = 5). (**k**) Immunofluorescence staining of STING (green) and DAPI staining (blue), scale bar = 10 $\mu$m. (**l**) Comparison of the integrated intensity of STING$^+$ (green) cells between two groups (n = 5). Two-tailed, unpaired t tests were conducted and the data are presented as the means ± SD, $^*p < 0.05$, $^{**}p < 0.01$. NRG1 neuregulin-1, *C* control1, *N* neuregulin-1, *DAPI* 4,6-Diamino-2-phenyl indole, *CD31* cluster of differentiation 31, *RIPK* receptor-interacting serine/threonine-protein kinase, *MLKL* mixed-lineage kinase domain-like, *STING* stimulator of interferon genes, *cGAS* cyclic GMP-AMP synthase

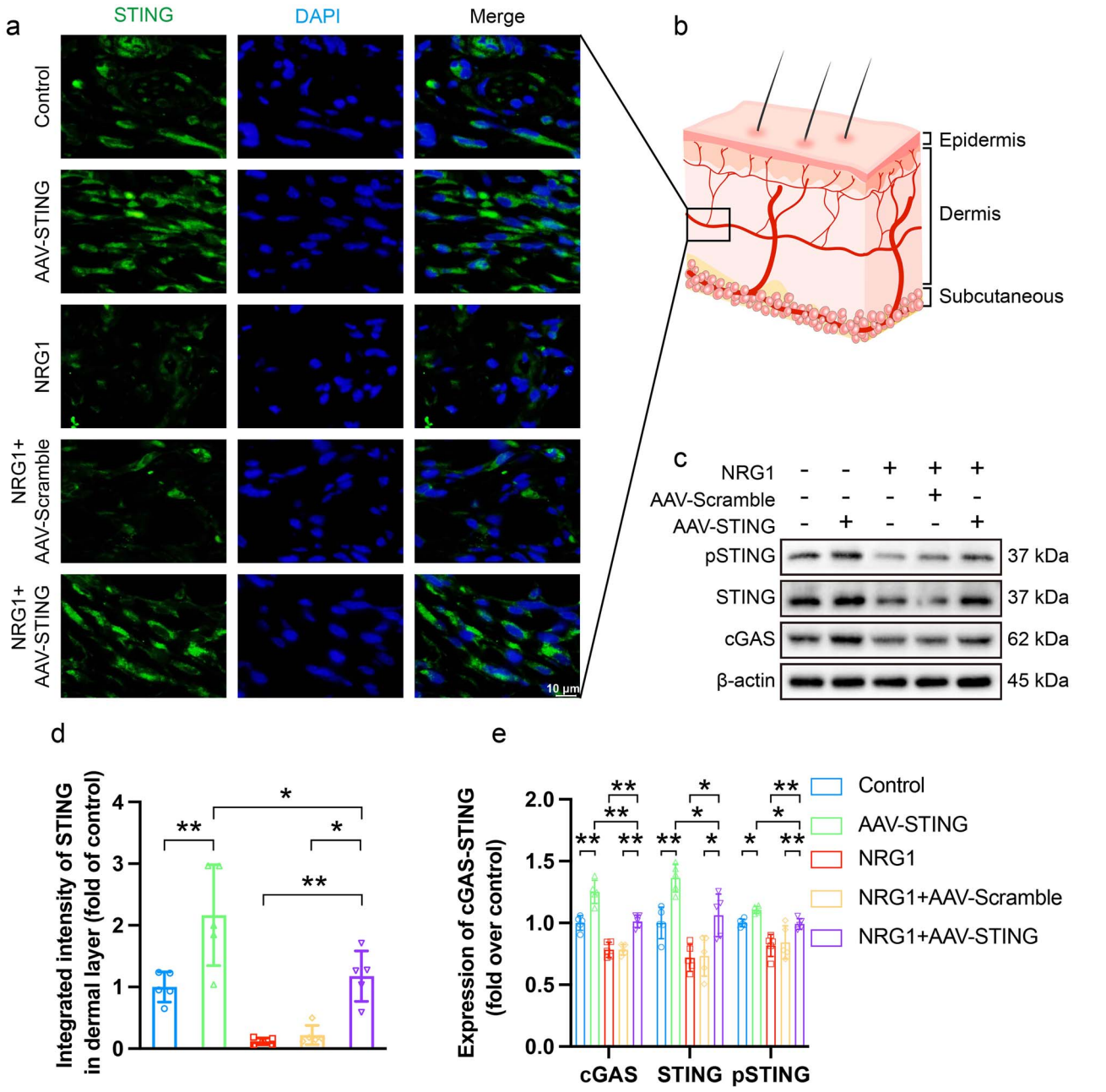


Figure 4. NRG1 inhibited STING activity in ischaemic flaps. (**a**,**b**,**d**) Immunofluorescence staining of STING (green) and DAPI staining (blue), scale bar = 10 $\mu$m. Comparison of the integrated intensity of STING$^{+}$ (green) cells among control, AAV-STING, NRG1, NRG1 + AAV-scramble, and NRG1 + AAV-STING groups (n = 5). (**c**) Western blot results of pSTING, STING and cGAS expression in the five groups presented as typical images. $\beta$-Actin was utilized as a loading control. (**e**) Quantification of the protein levels of pSTING, STING and cGAS. (n = 5). Statistical analysis was performed using ANOVA with the least significant difference *post hoc* test or Dunnett's T3 test. The data are presented as the means ± SD, $^{*}p < 0.05$, $^{**}p < 0.01$. *NRG1* neuregulin-1, *DAPI* 4,6-diamino-2-phenyl indole, *STING* stimulator of interferon genes, *cGAS* cyclic GMP-AMP synthase, AAV adeno-associated virus

activated the AKT-FOXO3a axis and increased FOXO3a levels in the cytoplasm, and these effects were reversed by MK-2206 (Fig. 7h, i). Furthermore, Western blotting results demonstrated that MK2206 markedly reversed NRG1-mediated inhibition of STING activity, pyroptosis and necroptosis through the AKT-FOXO3a signalling pathway. As illustrated in Fig. 7j–q, compared to the NRG1 group, the expression of pAKT and pFOXO3a in the ischemic flap were decreased in the NRG1 + MK2206 group. Meanwhile, the expression of pSTING, STING, cGAS, as well as pyroptosis-related proteins (GSDMD-N, NLRP3, cleaved-caspase1, ASC, IL-18 and IL-1$\beta$), and necroptosis-related proteins (RIPK1, RIPK3 and pMLKL) were increased. Additionally, the expression levels of pAKT and pFOXO3a in the NRG1 group were higher than that in the NRG1 + MK2206 group. Simultaneously, the expression levels of pSTING, STING, cGAS, as well as pyroptosis-related proteins and necroptosis-related proteins were lower in the NRG1 group than those in the NRG1 + MK2206 group. These results confirmed that NRG1 inhibited STING activity in ischaemic flaps through activating the AKT-FOXO3a signalling pathway.

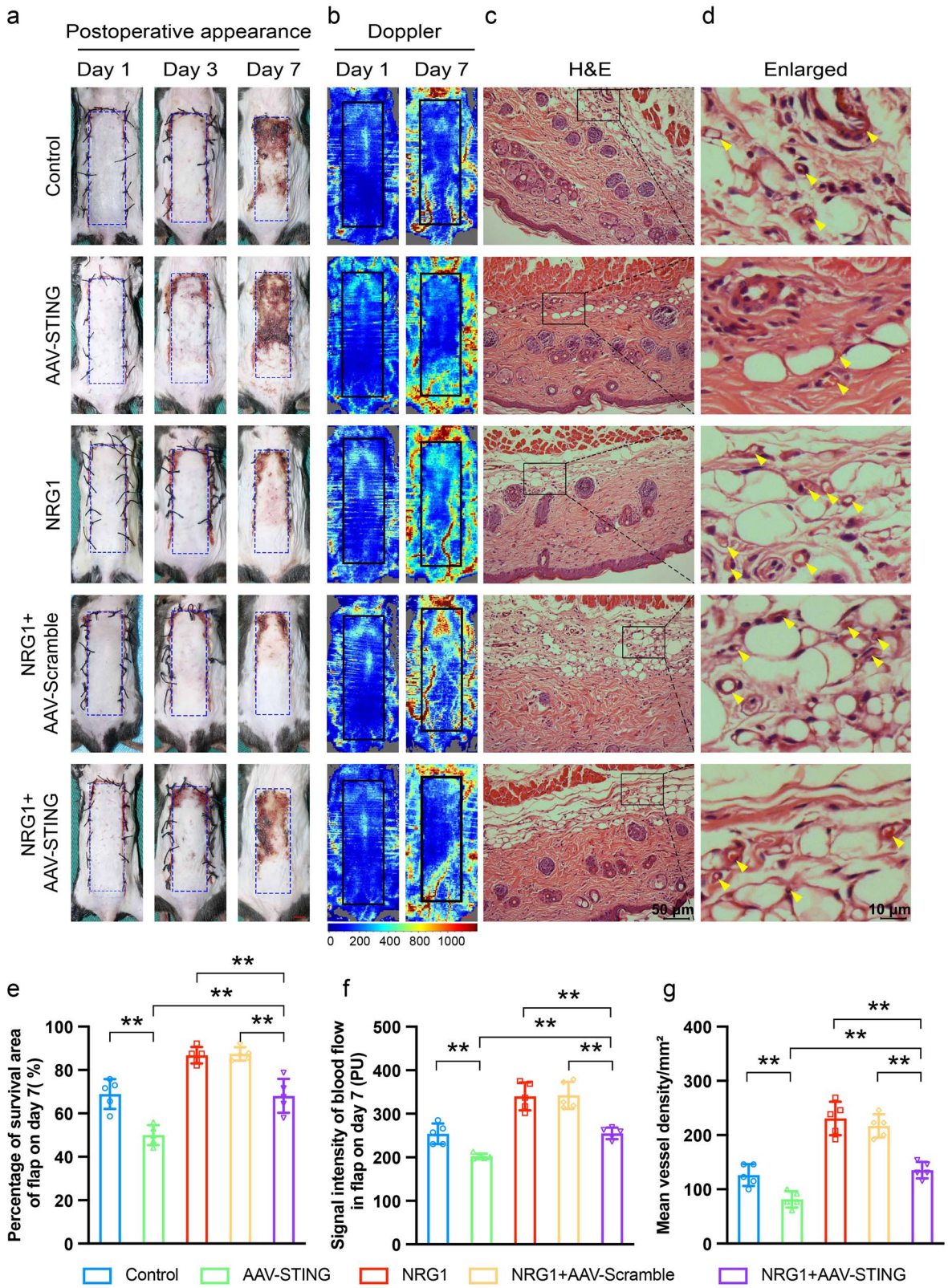


Figure 5. NRG1 promoted ischaemic flap survival by inhibiting STING activity. (**a**) Survival areas in control, AAV-STING, NRG1, NRG1 + AAV-scramble and NRG1 + AAV-STING groups on days 1, 3 and 7 after surgery. (**b**) LDBF analysis on days 1 and 7 after surgery. (**c**,**d**) H&E staining of skin tissues from zone-II of the flap in the five groups (scale bar = 50 $\mu$m, scale bar in the enlarged image = 10 $\mu$m). Yellow arrows indicating microvessels. (**e**) Comparison of the survival area among the five groups on day 7 (n = 5). (**g**) Comparison of the LDBF signals among the five groups on days 7 (n = 5). (**g**) Comparison of the mean vessel density (/mm$^2$) among the five groups (n = 5). Statistical analysis was performed using ANOVA with least significant difference *post hoc* tests or Dunnett's T3 test. The data are presented as the means ± SD, $^{**}p < 0.01$. *NRG1* neuregulin-1, *H&E* haematoxylin and eosin, *AAV* adeno-associated virus, *STING* stimulator of interferon genes

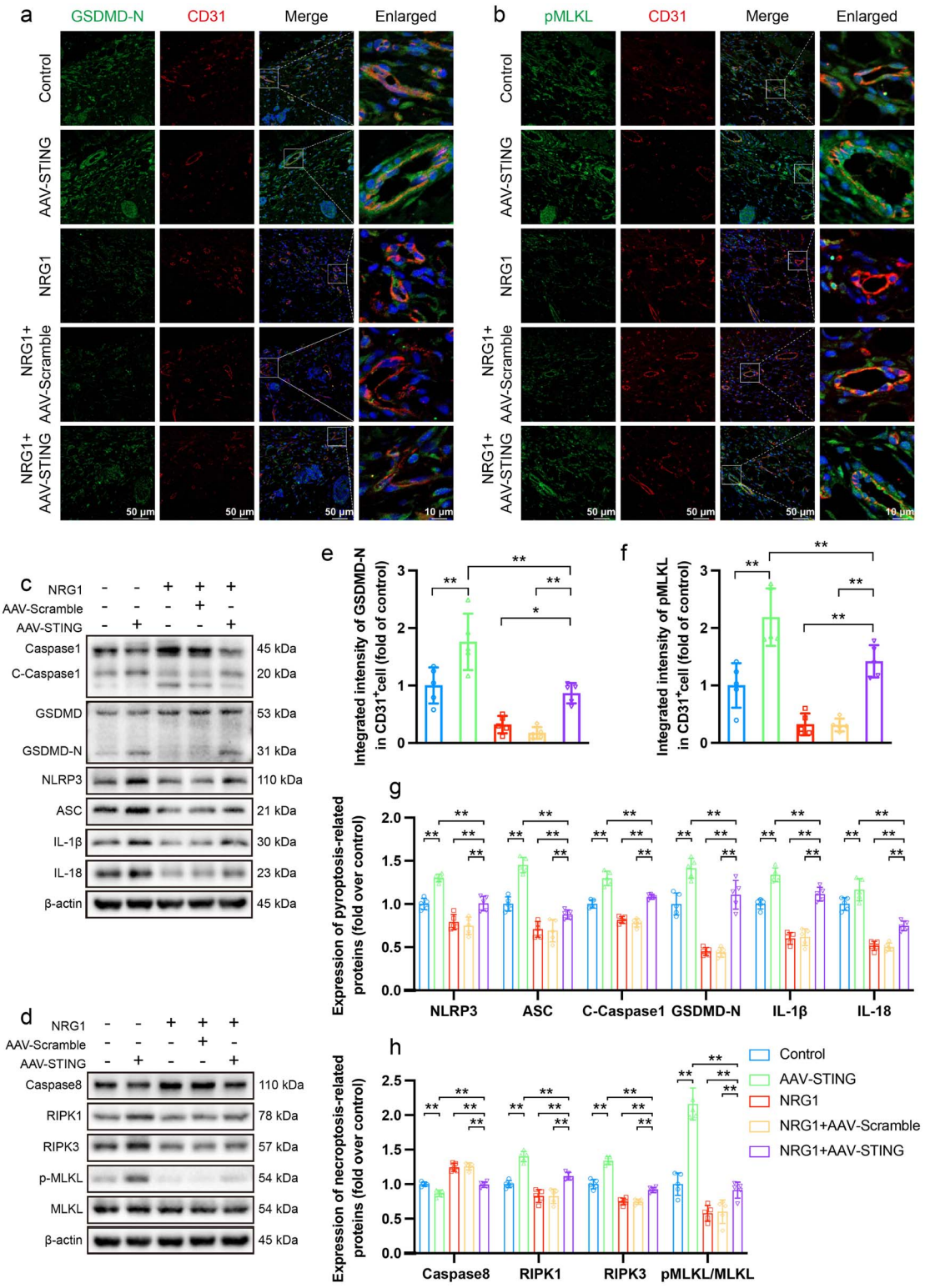


Figure 6. NRG1 decreased pyroptosis and necroptosis during ischaemic flap survival by inhibiting STING activity. (**a**) Immunofluorescence staining of GSDMD-N (green), CD31 (red) and DAPI staining (blue) (scale bar = 50 $\mu$m, scale bar in the enlarged image = 10 $\mu$m). (**b**) Immunofluorescence staining of pMLKL (green), CD31 (red) and DAPI (blue) (scale bar = 50 $\mu$m, scale bar in the enlarged image = 10 $\mu$m). (**c**) Western blot results of caspase1, GSDMD, ASC, NLRP3, IL-18 and IL-1$\beta$ expression in control, AAV-STING, NRG1, NRG1 + AAV-scramble, and NRG1 + AAV-STING groups presented as typical images. $\beta$-Actin was utilized as a loading control. (**d**) Western blot results of caspase8, RIPK1, RIPK3, MLKL and pMLKL expression in five groups presented as typical images. $\beta$-Actin was used as a loading control. (**e**) Comparison of the integrated intensity of GSDMD-N among the five groups (n = 5). (**f**) Comparison of the integrated intensity of pMLKL among the five groups (n = 5). (**g**) Quantification of the protein levels of cleaved-caspase1, GSDMD-N, ASC, NLRP3, IL-18 and IL-1$\beta$ (n = 5). (**h**) Quantification of the protein levels of caspase8, RIPK1, RIPK3 and pMLKL/MLKL (n = 5). Statistical analysis was performed using ANOVA with least significant difference *post hoc* tests or Dunnett's T3 test. The data are presented as the means ± SD, $^{*}p < 0.05$, $^{**}p < 0.01$. *NRG1* neuregulin-1, *AAV* adeno-associated virus, *STING* stimulator of interferon genes, *CD31* cluster of differentiation 31, *GSDMD* gasdermin D, *NLRP3* nucleotide-binding domain leucine-rich-containing family pyrin domain-containing-3, *ASC* adaptor apoptosis-associated speck-like protein containing a caspase-recruitment domain, *RIPK* receptor-interacting serine/threonine-protein kinase, *MLKL* mixed-lineage kinase domain-like

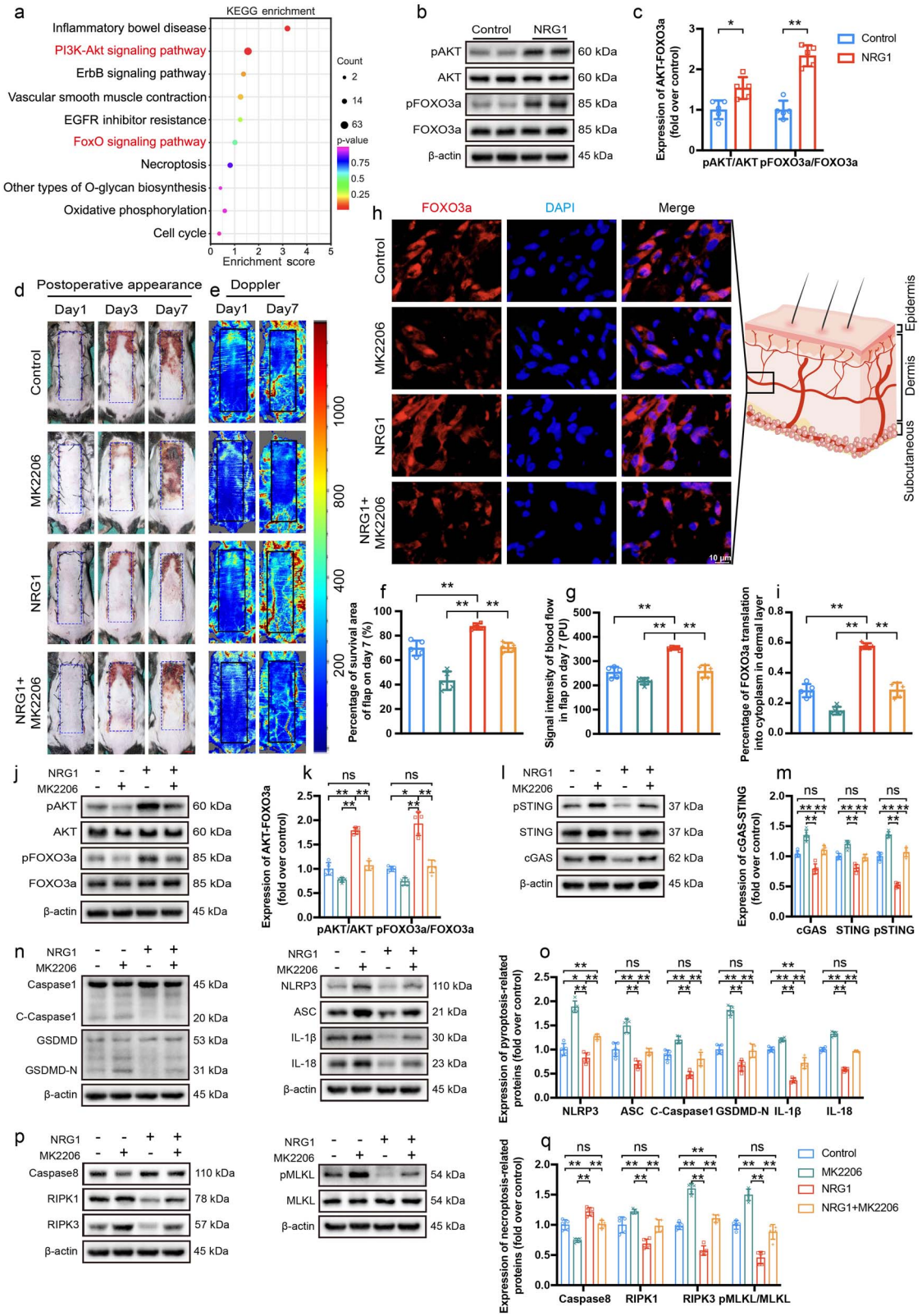


Figure 7. NRG1 inhibited STING activity via the AKT-FOXO3a signalling pathway. (**a**) KEGG enrichment plot displays pathways with statistically significant differences between the two groups related to AKT and NRG1. (**b**) Western blot results of AKT, pAKT, FOXO3a and pFOXO3a in control and NRG1 groups presented as typical images. $\beta$-Actin was utilized as a loading control. (**c**) Quantification of the protein levels of pAKT/AKT and pFOXO3a/FOXO3a (n = 5). (**d**) Survival areas of control, MK2206, NRG1 and NRG1 + MK2206 groups on days 1, 3 and 7 after surgery. (**e**) LDBF analysis of the four groups on days 1 and 7. (**f**) Comparison of the percentage of survival area on day 7 (n = 5). (**g**) Comparison of the LDBF signals among the four groups on day 7 (n = 5). (**h**) Immunofluorescence staining of FOXO3a (red) in skin tissue sections from dermal layer of the flap (scale bar = 10 $\mu$m). (**i**) Comparison of the FOXO3a$^+$ cells in the cytoplasm among the four groups (n = 5). (**j**) Western blot results of AKT, pAKT, FOXO3a and pFOXO3a in the four groups presented as typical images. (**k**) Quantification of the protein levels of pAKT/AKT and pFOXO3a/FOXO3a (n = 5). (**l**) Western blot results of pSTING, STING and cGAS in the four groups presented as typical images. (**m**) Quantification of the protein levels of pSTING, STING and cGAS (n = 5). (**n**) Western blot results of GSDMD,

## Discussion

Random pattern flap surgery is widely used in the field of wound repair. However, flaps with an inappropriate length-to-width ratio are prone to distal necrosis, substantially limiting the applicability of these flaps [40]. According to current research, the main causes of early distal flap necrosis are local ischaemia and surgical trauma [41]. Ischaemia leads to oxidative stress and cell death, while the subsequent inflammatory response further exacerbates oxidative stress and cell death, which is a crucial factor in the gradual necrosis of the flap after surgery [42]. The main objective of this study was to identify bioactive drugs that disrupt this vicious cycle, thereby promoting flap survival.

NRG1 belongs to the transmembrane growth factor family and is widely distributed in organisms. This molecule exerts systemic effects through the ErbB family of receptors, such as by inhibiting inflammatory responses, reducing oxidative stress, protecting central and peripheral nerve function and providing broad protection against various pathological conditions [43–46]. The greater biocompatibility of NRG1, an endogenous protein, makes it easier to combine with some common biomaterials to exert therapeutic effects. Hui used NRG1-loaded hydrogels to promote nerve regeneration and axonal remyelination in nerve defects [47], while Yoon *et al*. combined NRG1 with artificial dermis for the treatment of wound defects with encouraging results [25]. The potential therapeutic effects of NRG1 on ischaemic injury and wound repair have substantial research value. Interestingly, a multicentre, randomized controlled phase 2 clinical trial on recombinant human NRG1 has confirmed the safety and effectiveness of the protein in patients with chronic heart failure [48]. The latest clinical trial on NRG1 conducted in China showed that recombinant human NRG-1 is rapidly cleared from the blood, with a short half-life of ∼10 min, and related adverse reactions are mild, indicating that recombinant human NRG1 is safe and well tolerated in healthy Chinese subjects [49]. This evidence suggests that NRG1 has potential clinical application prospects. Our study, for the first time, applied NRG1 to the treatment of ischaemic flaps, and it was found that NRG1 promoted the survival of the ischaemic area of the flap. Furthermore, this study first verified that NRG1 inhibited the activation of STING through activating the AKT-FOXO3A pathway, thereby suppressing necroptosis, pyroptosis and oxidative stress while promoting angiogenesis, thus increasing the survival of the ischaemic areas of the flap. This outcome highlights the potential therapeutic advantages of NRG1 in the clinical field of flap repair.

Previous studies have demonstrated the positive role of angiogenesis in flap survival [50,51]. A good angiogenic capacity predicts the viability of flaps. The loss of angiogenesis in the ischaemic areas of the flap also suggests the collapse of the internal environment of the flap, which is unable to combat oxidative stress and cell death. NRG-1 regulates vascular growth factors, and previous data suggest that VEGF and angiopoietin-1 (Ang-1) regulate myocardial angiogenesis and growth through the NRG-1/ErbB signalling pathway [52]. The results from Hedhli *et al*. indicate that ligation of the femoral artery induces angiogenesis and arteriogenesis, with NRG-1 being a key factor in this process. Additionally, exogenous injection of NRG-1 promoted this process [53]. VEGF specifically promotes endothelial cell expansion, proliferation and migration and is directly associated with angiogenesis, while MMP9 is one of the major contributors to VEGF release and angiogenesis [54–56]. Furthermore, cadherin 5 promotes endothelial cell connections and prevents the destruction of newly formed vessels [57]. We used VEGF, MMPs and cadherin 5 as markers of angiogenesis to reflect the level of angiogenesis in the ischaemic areas of the flap, revealing its viability. Additionally, CD34 IHC and H&E staining provided a more intuitive display of the greater neovascularization in the NRG1 treatment group. Moreover, LDBF analysis showed that the blood flow signals in the NRG1 treatment group were significantly stronger than those in the control group on the seventh postoperative day, further confirming the ability of NRG1 to promote flap survival.

Inhibition of oxidative stress is needed to restore the viability of ischaemic flaps [32]. It was reported that NRG-1 reduced myocardial oxidative damage by regulating eNOS activity and protected myocardial tissue by inhibiting NADPH oxidase 4 through extracellular signal-regulated kinase 1/2 activation [23]. Antioxidative enzymes (such as SOD) are the main defence mechanisms of cells against oxidative damage, and factors involved in antioxidative damage also include HO1 and eNOS [58–60]. The expression of these three key proteins involved in antioxidative stress was increased in the NRG1 treatment group, and the IHC results of SOD1 were consistent with this finding. These results indicated that NRG1 treatment inhibited the level of oxidative stress in ischaemic flap. Previous studies have thoroughly demonstrated the important role of oxidative stress and angiogenesis levels within flaps [32,50,51]. Therefore, in this study, the oxidative stress level and angiogenesis level of flaps were used to evaluate the viability of random skin flaps to better reflect the status of the flaps.

Necroptosis and pyroptosis are two forms of PCD closely associated with inflammation [61]. Unlike the apoptotic shrinkage observed in apoptosis, the specific core proteins GSDMD and MLKL form pores in the cell membrane, ultimately leading to cell lysis and the release of various inflammatory factors and necrotic substances [61]. If these inflammatory factors and DAMPs are not appropriately regulated, they can induce pyroptosis and necroptosis, further exacerbating cell death [62]. Previous sequencing results confirmed the crucial roles of pyroptosis and necroptosis in the progression of flap necrosis. Therefore, we investigated whether the promotion of flap survival by NRG1 occurs

Figure 7. caspase1, NLRP3, ASC, IL-1$\beta$ and IL-18 in the four groups presented as typical images. (**o**) Quantification of the protein levels of GSDMD-N, cleaved-caspase1, NLRP3, ASC, IL-1$\beta$ and IL-18 (n = 5). (**p**) Western blot results of caspase8, RIPK1, RIPK3, MLKL and pMLKL in the four groups presented as typical images. (**q**) Quantification of the protein levels of caspase8, RIPK1, RIPK3 and pMLKL/MLKL (n = 5). Statistical analysis was performed using ANOVA with least squares difference *post hoc* tests or Dunnett's T3 test. Data are presented as means ± SD, ns stands for not significant, $^{*}p < 0.05$, $^{**}p < 0.01$. *NRG1* neuregulin-1, *KEGG* Kyoto encyclopedia of genes and genomes, *STING* stimulator of interferon genes, cGAS cyclic GMP-AMP synthase, *GSDMD* gasdermin D, *NLRP3* nucleotide-binding domain leucine-rich-containing family pyrin domain-containing-3, *ASC* adaptor apoptosis-associated speck-like protein containing a caspase-recruitment domain, *RIPK* receptor-interacting serine/threonine-protein kinase, *MLKL* mixed-lineage kinase domain-like, *AKT* protein kinase B, *FOXO3a* forkhead box O3a

through the inhibition of pyroptosis and necroptosis in ischaemic flaps, reversing the gradually uncontrollable necrosis caused by early ischaemic damage. NRG1 significantly reduced the expression of proteins associated with pyroptosis (including ASC, cleaved-caspase1, NLRP3, GSDMD-N, IL-18 and IL-1$\beta$) in ischaemic flaps. The classic pathway of cellular pyroptosis was assessed. This process is initiated by the oligomerization of NLRP3 and recruitment of the adaptor protein ASC, which activates the protease caspase1. Activated caspase1 can cleave GSDMD into its N-terminal domain, leading to oligomerization and insertion into the cell membrane, the formation of pores and the release of DAMPs, IL-18, IL-1$\beta$ and other inflammatory mediators [63]. As indicated by the western blotting results, the NRG1 group displayed a downregulation of ASC and NLRP3 expression, accompanied by a reduction in cleaved-caspase1 level. Furthermore, a pivotal protein indicative of pyroptosis, GSDMD-N, exhibited decreased expression, aligning with the alterations observed in IL-18 and IL-1$\beta$ levels. Additionally, the colocalization confocal fluorescence of caspase-1/CD31 and GSDMD-N/CD31 demonstrated significantly reduced fluorescence intensities of pyroptosis-related proteins on vascular endothelial cells in the NRG1 group. These results collectively demonstrated that NRG1 significantly inhibited pyroptosis within the flap. After NRG1 treatment, the expression of necroptosis-related proteins (such as RIPK1, RIPK3 and pMLKL) also decreased. Necroptosis programmes are triggered downstream of death domain receptors (such as tumour necrosis factor receptor and Fas cell surface death receptor) and Toll-like receptor 4 or 3 [64–66]. Upon activation, these receptors recruit the adaptor proteins, which then interact with RIPK1 and caspase8 or caspase10 [67,68]. Upon detection of 'death signals', RIPK1 is activated and recruits RIPK3. The RIPK1/RIP3 complex recruits and phosphorylates MLKL. Phosphorylated MLKL oligomerizes to form necrosomes, which translocate to the plasma membrane and form large pores [69,70]. Ultimately, MLKL pores allow ion influx, cell swelling and membrane dissolution, leading to necrotic cell death, followed by the uncontrolled release of intracellular substances. Previous study has shown that microbes or drugs can trigger necroptosis by inhibiting the proteolytic enzyme caspase8 [71]. In the absence of caspase8 activity, RIPK1 recruits and phosphorylates RIPK3, forming a complex called the ripoptosome [72,73]. This finding was also confirmed in the present study, where after NRG1 treatment, the expression of caspase8 was upregulated, while the expression of RIPK1 and RIPK3 was downregulated, indicating a decrease in the expression of the ripoptosome complex. Concurrently, the expression of pMLKL decreased. Additionally, the confocal fluorescence of RIPK3/CD31 and pMLKL/CD31 colocalization demonstrated significantly reduced fluorescence intensities of necroptosis-related proteins on vascular endothelial cells in the NRG1 group. These results indicated that NRG1 effectively inhibited necroptosis in ischaemic flaps.

To explain how NRG1 promotes random flap viability, we further explored potential upstream mechanisms regulating pyroptosis and necroptosis. Previous study has shown that the cGAS-STING signalling axis plays an essential role in modulation of pyroptosis and necroptosis [36]. The cGAS-STING cell signalling axis is activated upon detection of pathogenic DNA, triggering innate immune responses. It is also activated by endogenous DNA [17]. Therefore, cGAS-STING has been identified as an essential axis involved in the sterile inflammatory response, autoimmunity and cell senescence [16]. Cytoplasmic DNA induces activation of the classic NLRP3 inflammasome [74]. This process is mainly characterized by the secretion of mature caspase1 or IL-1$\beta$ and the formation of membrane pores [74]. Intriguingly, researchers have also proposed that caspase1 or IL-1$\beta$ activation is mostly abrogated in cGAS- or STING-deficient cells [75]. Once activated, STING tends to target lysosomes, ultimately leading to destruction and lysosomal cell death [76]. These findings suggested that the cGAS/STING/lysosomal cell death/NLRP3 axis induces proinflammatory responses and pyroptosis related to cytoplasmic DNA [77]. Other recent studies have also highlighted the essential role of the STING axis in necroptosis regulation [36,78]. The cGAS-STING axis was proposed to induce cell necroptosis in principle macrophages [18]. Notably, cell death requires STING-dependent production of various molecules, such as tumour necrosis factor and type I IFNs, while cGAS-STING activation-induced necroptosis involves mutual and cooperative signal transduction of these two molecules [79]. In addition, Zhang's laboratory recently reported that after induction of necrosis, the release of cytoplasmic mitochondrial DNA (mtDNA) and subsequent activation of STING synergically promote the type I IFN response, inducing phosphorylation of RIPK3/MLKL to trigger necroptosis [80]. The transcriptome sequencing results revealed a significant difference in STING1 expression between the NRG1 treatment group and the control group. Subsequently, the levels of cGAS-STING signalling pathway components in random skin flaps were evaluated. The protein expression of cGAS-STING was significantly downregulated in the NRG1 treatment group. Additionally, the expression of STING in the dermal region of the flap was assessed by immunofluorescence, and the fluorescence intensity in the NRG1 group decreased significantly. These findings indicate that NRG1 inhibited the activity of STING in ischaemic flaps. To validate the relationship between the inhibition of STING and pyroptosis and necroptosis, AAV-STING was used to upregulate the expression of STING in a mouse model of ischaemic flaps. After AAV-STING upregulation, pyroptosis and necroptosis were increased, and the survival capacity of the flap decreased. Additionally, an AAV-STING+NRG1 group was established. Compared to NRG1 alone, AAV-STING reversed the positive effects of NRG1 on the flap, further demonstrating that NRG1 suppresses pyroptosis and necroptosis by inhibiting STING, thereby promoting flap survival. This is the first study to combine the activity of STING with random skin flap necrosis, providing ground-breaking insights for future research on flap ischaemic necrosis.

Given the favourable therapeutic potential of NRG1, we next explored how NRG1 promotes STING activity to obtain more reliable evidence for future potential clinical applications. Recent studies on neural stem cells have shown that FOXO3 activation activates the cGAS-STING signalling axis [81]. FOXO transcription factors, including FOXO-1, FOXO-3, FOXO-4 and FOXO-6, are key regulators of target genes involved in the cell cycle, cell death and cell differentiation [82]. Activated forkhead members mainly act as tumour suppressors, promoting cell cycle arrest and cell death [83]. When forkhead transcription factors are AKT-phosphorylated and inactivated, cell proliferation increases, leading to nucleation and blockage of transcription factor activity [84]. Moreover, AKT kinase has been shown to play a negative role in

cGAS-mediated antiviral immune responses and is one of the most essential and broadly functional protein kinases in eukaryotes [16]. Many AKT substrates are involved in cell survival, metabolism, migration and proliferation [85]. Recent studies on spinal cord injury and Charcot-Marie-Tooth revealed that the repair effect of NRG1 was most strongly associated with AKT activation [86,87]. Furthermore, KEGG enrichment analysis revealed a significant difference in the AKT pathway and FOXO pathway between the two groups (Fig. 7a). Therefore, we speculated that NRG1 might inhibit STING by activating the AKT-FOXO3a axis. The results, shown in Fig. 7b, demonstrated increased phosphorylation of AKT at Ser473 and increased phosphorylation of FOXO3a at Thr32 in the NRG1 group, revealing that NRG1 activated the AKT-FOXO3a pathway within flap tissue. For confirmation of the relationship between the activation of AKT-FOXO3a within the flap and the inhibition of STING activity, MK-2206 was used as an AKT inhibitor to suppress the activation of the NRG1-mediated AKT-FOXO3a signalling pathway. Compared to the NRG1 group, the NRG1 + MK2206 group showed suppressed activation of the AKT-FOXO3a signalling pathway, a rebound in STING expression, and an increase in cellular pyroptosis and necroptosis. MK2206 treatment reversed the positive effects of NRG1 on the flap. In conclusion, for the first time, in flap tissue, we demonstrated that NRG1 inhibited pyroptosis and necroptosis by suppressing STING activity through the AKT-FOXO3a pathway.

This study also has several limitations. (1) GO analysis of the RNA sequencing results revealed a potential inhibition of the nuclear factor kappa-light-chain-enhancer of activated B cells (NF-$\kappa$B) signalling pathway in the experimental group. NF-$\kappa$B is a key regulatory factor of the $\kappa$B light chain in B cells and is closely associated with diseases, inflammation and the immune system's perception of pathogens [88]. We did not investigate the function of NF-$\kappa$B in flap necrosis, yet previous research has shown that activation of STING can stimulate NF-$\kappa$B activity, which is also linked to pyroptosis and necroptosis [76]. Therefore, the NF-$\kappa$B cellular signalling pathway is also a worthy direction for further studies of the flap necrosis mechanisms. (2) Various types of cells, such as endothelial cells, adipocytes, fibroblasts and neutrophils (which infiltrate during inflammation), exist in the dermis of mammalian skin. Understanding which cell type undergoes pyroptosis and necroptosis first will be crucial, as this knowledge will help us better comprehend the pathological process of ischaemic flaps. The current study does not yet provide answers to this question, but it will be a valuable research direction in the future using advanced techniques such as single-cell sequencing and spatial transcriptomics.

## Conclusions

This study showed that NRG1 inhibits pyroptosis and necroptosis by activating the AKT/FOXO3a signalling pathway to suppress STING activation and promote ischaemic flap survival. Therefore, it is proposed that NRG1 has good potential for future clinical applications.

## Abbreviations

AAV: Adeno-associated virus; AKT: Protein kinase B; ASC: Apoptosis-associated speck-like protein containing a caspase-recruitment domain; CD34: Cluster of differentiation 34; cGAS: Cyclic GMP-AMP synthase; DAPI: 4, 6-Diamino-2-phenyl indole; DEG: Differentially expressed gene; ELISA: Enzyme-linked immunosorbent assay; eNOS: Endothelial nitric oxide synthase; FOXO3a: Forkhead box O3a; GO: Gene ontology; GSDMD: Gasdermin D; HO1: Heme oxygenase 1; H&E: Haematoxylin and eosin; IFN: Interferon; IHC: Immunohistochemistry; LDBF: Laser Doppler blood flow; MLKL: Mixed lineage kinase domain-like protein; MMP9: Matrix metalloproteinase 9; NLRP3: Nucleotide-binding domain leucine-rich-containing family pyrin domain-containing-3; NRG1: Neuregulin-1; RIPKs: Receptor-interacting protein kinases; SDS–PAGE: Sodium dodecyl sulfate–polyacrylamide gel electrophoresis; SOD1: Superoxide dismutase 1; VEGF: Vascular endothelial growth factor; PCD: Programmed cell death; TMEM173: Transmembrane protein 173; MITA: Mediator of IRF3 activation; PBS: Phosphate-buffered saline; BSA: Bovine serum albumin; HRP: Horseradish peroxidase; BCA: Bicinchoninic acid; SC buffer: Sodium citrate buffer; DTIAS: Dual targeted intracellular activity sensor; PVDF: Polyvinylidene fluoride; mRNA LT: Messenger RNA long transcript; ANOVA: Analysis of variance; Ang-1: Angiopoietin-1; mtDNA: Mitochondrial DNA; NF-kB: Nuclear factor kappa-light-chain-enhancer of activated B cells; DAB: 3,3′-diaminobenzidine

## Acknowledgements

This work was supported by grants from National Natural Science Foundation of China (No. 82372540 and 82072192 to KZ, No. 81801930 to JD, No. 81873942 to WG); Public Welfare Technology Research Project of Zhejiang Province (No. LGF20H150003 to KZ, No. LQ23H090006 to Ya Lv); and Wenzhou Science and Technology Bureau Foundation (No. Y20210438 to KZ, No. Y2023475 to XZ).

## Supplementary data

Supplementary data is available at *Burns & Trauma Journal* online.

## Funding

This work was supported by the Natural Science Foundation of China [82372540, 82072192, 81801930, 81873942]; Wenzhou Science and Technology Bureau Foundation [Y20210438; Y2023475]; Public Welfare Technology Research Project of Zhejiang Province [LGF20H150003; LQ23H090006]; Basic Public Welfare Research Project of Zhejiang Province [No.LY19H060003]; and Medical Health Science and Technology Project of Zhejiang Province [No. 2020KY183].

## Authors' contributions

Xuwei Zhu (Conceptualization [equal], Data curation [equal], Formal analysis [equal], Funding acquisition [supporting], Investigation [equal], Methodology [equal], Validation [equal], Writing—original draft [equal]), Gaoxiang Yu (Data curation [equal], Formal analysis [equal], Investigation [equal], Methodology [equal], Validation [equal], Writing—original draft [equal]), Ya Lv (Data curation [equal], Formal analysis [equal], Funding acquisition [equal], Investigation [equal], Methodology [equal]), Ningning Yang (Data curation [equal], Formal analysis [equal], Investigation [equal], Methodology [equal]), Yinuo Zhao (Data curation [equal], Formal analysis [equal], Methodology [equal]), Feida Li (Data curation [equal], Formal analysis [equal], Methodology [equal], Jiayi Zhao (Formal analysis [equal], Methodology [equal]), Zhuliu Chen (Formal analysis [equal], Methodology

[equal]), Yingying Lai (Investigation [equal], Methodology [equal]), Liang Chen (Investigation [equal], Methodology [equal]), Xiangyang Wang (Resources [supporting], Writing—review & editing [supporting]), Jian Xiao (Supervision [supporting], Writing—review & editing [supporting]), Yuepiao Cai (Validation [supporting], Writing—review & editing [supporting]), Yongzeng Feng (Conceptualization [equal], Supervision [equal], Validation [equal], Visualization [equal], Writing—review & editing [equal]), Jian Ding (Funding acquisition [equal], Project administration [equal], Supervision [equal], Validation [equal], Visualization [equal], Writing—review & editing [equal], Weiyang Gao (Conceptualization [equal], Funding acquisition [equal], (Project administration [equal], Resources [equal], Software [equal], Supervision [equal], Validation [equal], Writing—review & editing [equal]), Kailiang Zhou (Conceptualization [equal], Funding acquisition [equal], Investigation [equal], Project administration [equal], Resources [equal], Software [equal], Supervision [equal], Validation [equal], Visualization [equal], Writing—review & editing [equal]), and Hui Xu (Conceptualization [equal], Project administration [equal], Resources [equal], Software [supporting], Validation [equal], Visualization [equal], Writing—review & editing [equal]).

## Ethics approval

All experiments involving animals were conducted according to the ethical policies and procedures approved by the ethics committee of Wenzhou Medical University (WYDW 2024–0058).

## Conflict of interest

None declared.

## Data availability

Additional data collected during this study are available from the corresponding author upon reasonable request.

## References


1. Charafeddine AH, Drake R, McBride J. *et al.* Facelift: History and Anatomy. *Clin Plast Surg* 2019;**46**:505–13.
2. Summers BK, Siegle RJ. Facial cutaneous reconstructive surgery: general aesthetic principles. *J Am Acad Dermatol* 1993;**29**:669–81.
3. Chung S, Hazen A, Levine JP. *et al.* Vascularized acellular dermal matrix island flaps for the repair of abdominal muscle defects. *Plast Reconstr Surg* 2003;**111**:225–32.
4. Chen Z, Wu H, Yang J. *et al.* Activating Parkin-dependent mitophagy alleviates oxidative stress, apoptosis, and promotes random-pattern skin flaps survival. *Communications Biology* 2022;**5**:616.
5. Weinzierl A, Ampofo E, Menger MD. *et al.* Tissue-Protective Mechanisms of Bioactive Phytochemicals in Flap Surgery. *Front Pharmacol* 2022;**13**:864351. https://doi.org/10.3389/fphar.2022.864351.
6. Man SM, Karki R, Kanneganti T-D. Molecular mechanisms and functions of pyroptosis, inflammatory caspases and inflammasomes in infectious diseases. *Immunol Rev* 2017;**277**:61–75.
7. Chen D-Q, Guo Y, Li X. *et al.* Small molecules as modulators of regulated cell death against ischemia/reperfusion injury. *Med Res Rev* 2022;**42**:2067–101.
8. Wu L, Zhao H, Zhang M. *et al.* Regulated cell death and inflammasome activation in gut injury following traumatic surgery in vitro and in vivo: implication for postoperative death due to multiorgan dysfunction. *Cell Death Discovery* 2023;**9**:409.
9. Shi J, Gao W, Shao F. Pyroptosis: Gasdermin-Mediated Programmed Necrotic Cell Death. *Trends Biochem Sci* 2017;**42**:245–54.
10. Sun Y-B, Zhao H, Mu D-L. *et al.* Dexmedetomidine inhibits astrocyte pyroptosis and subsequently protects the brain in in vitro and in vivo models of sepsis. *Cell Death Dis* 2019;**10**:167.
11. Zhao H, Ning J, Lemaire A. *et al.* Necroptosis and parthanatos are involved in remote lung injury after receiving ischemic renal allografts in rats. *Kidney Int* 2015;**87**:738–48.
12. Lou J, Wang X, Zhang H. *et al.* Inhibition of PLA2G4E/cPLA2 promotes survival of random skin flaps by alleviating Lysosomal membrane permeabilization-Induced necroptosis. *Autophagy* 2022;**18**:1841–63.
13. Galluzzi L, Kepp O, Chan FK-M. *et al.* Necroptosis: Mechanisms and Relevance to Disease. *Annu Rev Pathol* 2017;**12**:103–30.
14. Lou J, Zhang H, Qi J. *et al.* Cyclic helix B peptide promotes random-pattern skin flap survival via TFE3-mediated enhancement of autophagy and reduction of ROS levels. *Br J Pharmacol* 2022;**179**:301–21.
15. Li Q, Chen Q, Yang X. *et al.* Cocktail strategy based on a dual function nanoparticle and immune activator for effective tumor suppressive. *Journal of Nanobiotechnology* 2022;**20**:84.
16. Oduro PK, Zheng X, Wei J. *et al.* The cGAS-STING signaling in cardiovascular and metabolic diseases: Future novel target option for pharmacotherapy. *Acta Pharm Sin B* 2022;**12**:50–75.
17. Hu Q, Ren H, Li G. *et al.* STING-mediated intestinal barrier dysfunction contributes to lethal sepsis. *EBioMedicine* 2019;**41**:497–508.
18. Luo W, Wang Y, Zhang L. *et al.* Critical Role of Cytosolic DNA and Its Sensing Adaptor STING in Aortic Degeneration, Dissection, and Rupture. *Circulation* 2020;**141**:42–66.
19. Bartus K, Galino J, James ND. *et al.* Neuregulin-1 controls an endogenous repair mechanism after spinal cord injury. *Brain* 2016;**139**:1394–416.
20. Figliolini F, Ranghino A, Grange C. *et al.* Extracellular Vesicles From Adipose Stem Cells Prevent Muscle Damage and Inflammation in a Mouse Model of Hind Limb Ischemia: Role of Neuregulin-1. *Arterioscler Thromb Vasc Biol* 2020;**40**:239–54.
21. Kang W, Cheng Y, Wang X. *et al.* Neuregulin-1: An underlying protective force of cardiac dysfunction in sepsis (Review). *Mol Med Rep* 2020;**21**:2311–20.
22. Hedhli N, Huang Q, Kalinowski A. *et al.* Endothelium-derived neuregulin protects the heart against ischemic injury. *Circulation* 2011;**123**:2254–62.
23. Wang F, Wang H, Liu X. *et al.* Neuregulin-1 alleviate oxidative stress and mitigate inflammation by suppressing NOX4 and NLRP3/caspase-1 in myocardial ischaemia-reperfusion injury. *J Cell Mol Med* 2021;**25**:1783–95.
24. Jarde T, Chan WH, Rossello FJ. *et al.* Mesenchymal Niche-Derived Neuregulin-1 Drives Intestinal Stem Cell Proliferation and Regeneration of Damaged Epithelium. *Cell Stem Cell* 2020;**27**:646–662.e7.
25. Yoon D, Yoon D, Cha HJ. *et al.* Enhancement of wound healing efficiency mediated by artificial dermis functionalized with EGF or NRG1. *Biomed Mater* 2018;**13**:045007. https://doi.org/10.1088/1748-605X/aaac37.
26. Wu S, Zhang Q, Zhang F. *et al.* HER2 recruits AKT1 to disrupt STING signalling and suppress antiviral defence and antitumour immunity. *Nat Cell Biol* 2019;**21**:1027–40.
27. Zhou K, Chen H, Lin J. *et al.* FGF21 augments autophagy in random-pattern skin flaps via AMPK signaling pathways and improves tissue survival. *Cell Death Dis* 2019;**10**:872.
28. Lou J, Wang X, Zhang H. *et al.* Inhibition of PLA2G4E/cPLA2 promotes survival of random skin flaps by alleviating Lysosomal membrane permeabilization-Induced necroptosis. *Autophagy* 2021;**18**:1841–63.
29. Li J, Chen H, Lou J. *et al.* Exenatide improves random-pattern skin flap survival via TFE3 mediated autophagy augment. *J Cell Physiol* 2021;**236**:3641–59.
30. Liu M, Solomon W, Cespedes JC. *et al.* Neuregulin-1 attenuates experimental cerebral malaria (ECM) pathogenesis by regulating ErbB4/AKT/STAT3 signaling. *J Neuroinflammation* 2018;**15**:104.

31. Hirai H, Sootome H, Nakatsuru Y. *et al.* MK-2206, an allosteric Akt inhibitor, enhances antitumor efficacy by standard chemotherapeutic agents or molecular targeted drugs in vitro and in vivo. *Mol Cancer Ther* 2010;**9**:1956–67.
32. Odake K, Tsujii M, Iino T. *et al.* Febuxostat treatment attenuates oxidative stress and inflammation due to ischemia-reperfusion injury through the necrotic pathway in skin flap of animal model. *Free Radic Biol Med* 2021;**177**:238–46.
33. Li J, Lou J, Yu G. *et al.* Targeting TFE3 Protects Against Lysosomal Malfunction-Induced Pyroptosis in Random Skin Flaps via ROS Elimination. *Frontiers In Cell and Developmental Biology* 2021;**9**:643996. https://doi.org/10.3389/fcell.2021.643996.
34. Yang N, Yu G, Lai Y. *et al.* A snake cathelicidin enhances transcription factor EB-mediated autophagy and alleviates ROS-induced pyroptosis after ischaemia-reperfusion injury of island skin flaps. *Br J Pharmacol* 2024;**181**:1068–90.
35. Zhang T, Wang Y, Inuzuka H. *et al.* Necroptosis pathways in tumorigenesis. *Semin Cancer Biol* 2022;**86**:32–40.
36. Hu X, Zhang H, Zhang Q. *et al.* Emerging role of STING signalling in CNS injury: inflammation, autophagy, necroptosis, ferroptosis and pyroptosis. *J Neuroinflammation* 2022;**19**:242.
37. Qiao J, Sun J, Chen L. *et al.* Neuregulin-1/ErbB4 upregulates acetylcholine receptors via Akt/mTOR/p70S6K: a study in a rat model of obstetric brachial plexus palsy and. *Acta Biochim Biophys Sin* 2022;**54**:1648–57.
38. Yoo J-Y, Kim H-B, Baik T-K. *et al.* Neuregulin 1/ErbB4/Akt signaling attenuates cytotoxicity mediated by the APP-CT31 fragment of amyloid precursor protein. *Exp Mol Pathol* 2021;**120**:104622. https://doi.org/10.1016/j.yexmp.2021.104622.
39. Shen Q, Yang L, Li C. *et al.* Metformin promotes cGAS/STING signaling pathway activation by blocking AKT phosphorylation in gastric cancer. *Heliyon* 2023;**9**(**8**):e18954. https://doi.org/10.1016/j.heliyon.2023.e18954.
40. Zhu D, Chen B, Xiang Z. *et al.* Apigenin enhances viability of random skin flaps by activating autophagy. *Phytotherapy Research : PTR* 2021;**35**:3848–60.
41. Zhang D, Yuan Y, Zhang H. *et al.* Photoacoustic Microscopy Provides Early Prediction of Tissue Necrosis in Skin Avulsion Injuries. *Clin Cosmet Investig Dermatol* 2021;**Volume 14**: 837–44.
42. Jiang J, Dong C, Zhai L. *et al.* Paeoniflorin Suppresses TBHP-Induced Oxidative Stress and Apoptosis in Human Umbilical Vein Endothelial Cells via the Nrf2/HO-1 Signaling Pathway and Improves Skin Flap Survival. *Front Pharmacol* 2021;**12**:735530. https://doi.org/10.3389/fphar.2021.735530.
43. Wang X, Zhuo X, Gao J. *et al.* Neuregulin-1beta Partially Improves Cardiac Function in Volume-Overload Heart Failure Through Regulation of Abnormal Calcium Handling. *Front Pharmacol* 2019;**10**:616.
44. Wang X, Liu Z, Duan HN. *et al.* Therapeutic Potential of Neuregulin in Cardiovascular System: Can we Ignore the Effects of Neuregulin on Electrophysiology? *Mini Rev Med Chem* 2016;**16**: 867–71.
45. Jabbour A, Hayward CS, Keogh AM. *et al.* Parenteral administration of recombinant human neuregulin-1 to patients with stable chronic heart failure produces favourable acute and chronic haemodynamic responses. *Eur J Heart Fail* 2011;**13**: 83–92.
46. Gonkowski S. Neuregulin 1 (NRG1) and its receptors in the enteric nervous system and other parts of the gastrointestinal wall. *Histol Histopathol* 2024;18721. https://doi.org/10.14670/HH-18-721.
47. Hui T, Wang C, Yu L. *et al.* Phosphorene hydrogel conduits as "neurotrophin reservoirs" for promoting regeneration of peripheral nerves. *J Mater Chem B* 2023;**11**:3808–15.
48. Gao R, Zhang J, Cheng L. *et al.* A Phase II, randomized, double-blind, multicenter, based on standard therapy, placebo-controlled study of the efficacy and safety of recombinant human neuregulin-1 in patients with chronic heart failure. *J Am Coll Cardiol* 2010;**55**: 1907–14.
49. Xu J, Sun P, Zhao X. *et al.* Safety, Tolerability, and Pharmacokinetics of Recombinant Human Neuregulin-1 in Healthy Chinese Subjects. *Am J Cardiovasc Drugs* 2023;**23**:419–28.
50. Zhu X, Hu X, Lou J. *et al.* Liraglutide, a TFEB-Mediated Autophagy Agonist, Promotes the Viability of Random-Pattern Skin Flaps. *Oxidative Med Cell Longev* 2021;**2021**: 6610603–18.
51. He JB, Ma XY, Li WJ. *et al.* Exenatide inhibits necrosis by enhancing angiogenesis and ameliorating ischemia/reperfusion injury in a random skin flap rat model. *Int Immunopharmacol* 2021;**90**:107192. https://doi.org/10.1016/j.intimp.2020.107192.
52. Gui C, Zeng ZY, Chen Q. *et al.* Neuregulin-1 Promotes Myocardial Angiogenesis in the Rat Model of Diabetic Cardiomyopathy. *Cell Physiol Biochem* 2018;**46**:2325–34.
53. Hedhli N, Dobrucki LW, Kalinowski A. *et al.* Endothelial-derived neuregulin is an important mediator of ischaemia-induced angiogenesis and arteriogenesis. *Cardiovasc Res* 2012;**93**:516–24.
54. Xu B, Iida Y, Glover KJ. *et al.* Inhibition of VEGF (Vascular Endothelial Growth Factor)-A or its Receptor Activity Suppresses Experimental Aneurysm Progression in the Aortic Elastase Infusion Model. *Arterioscler Thromb Vasc Biol* 2019;**39**:1652–66.
55. Ahmad A, Nawaz MI. Molecular mechanism of VEGF and its role in pathological angiogenesis. *J Cell Biochem* 2022;**123**:1938–65.
56. Swetha R, Gayen C, Kumar D. *et al.* Biomolecular basis of matrix metallo proteinase-9 activity. *Future Med Chem* 2018;**10**: 1093–112.
57. Krishna K, Redies C. Expression of cadherin superfamily genes in brain vascular development. *J Cereb Blood Flow Metab* 2009;**29**: 224–9.
58. Xu J, Su X, Burley SK. *et al.* Nuclear SOD1 in Growth Control, Oxidative Stress Response, Amyotrophic Lateral Sclerosis, and Cancer. *Antioxidants (Basel)* 2022;**11**. https://doi.org/10.3390/antiox11020427.
59. Chiang SK, Chen SE, Chang LC. The Role of HO-1 and Its Crosstalk with Oxidative Stress in Cancer Cell Survival. *Cells* 2021;**10**. https://doi.org/10.3390/cells10092401.
60. Li H, Horke S, Forstermann U. Oxidative stress in vascular disease and its pharmacological prevention. *Trends Pharmacol Sci* 2013;**34**:313–9.
61. Tang R, Xu J, Zhang B. *et al.* Ferroptosis, necroptosis, and pyroptosis in anticancer immunity. *J Hematol Oncol* 2020;**13**:110.
62. Zhang Q, Jia M, Wang Y. *et al.* Cell Death Mechanisms in Cerebral Ischemia-Reperfusion Injury. *Neurochem Res* 2022;**47**:3525–42.
63. Shi J, Zhao Y, Wang K. *et al.* Cleavage of GSDMD by inflammatory caspases determines pyroptotic cell death. *Nature* 2015;**526**: 660–5.
64. He S, Liang Y, Shao F. *et al.* Toll-like receptors activate programmed necrosis in macrophages through a receptor-interacting kinase-3-mediated pathway. *Proc Natl Acad Sci USA* 2011;**108**: 20054–9.
65. Kaiser WJ, Sridharan H, Huang C. *et al.* Toll-like receptor 3-mediated necrosis via TRIF, RIP3, and MLKL. *J Biol Chem* 2013;**288**:31268–79.
66. Lim J, Park H, Heisler J. *et al.* Autophagy regulates inflammatory programmed cell death via turnover of RHIM-domain proteins. *elife* 2019;**8**:8.
67. Tenev T, Bianchi K, Darding M. *et al.* The Ripoptosome, a signaling platform that assembles in response to genotoxic stress and loss of IAPs. *Mol Cell* 2011;**43**:432–48.
68. Feoktistova M, Geserick P, Kellert B. *et al.* cIAPs block Ripoptosome formation, a RIP1/caspase-8 containing intracellular cell death complex differentially regulated by cFLIP isoforms. *Mol Cell* 2011;**43**:449–63.
69. Zhao J, Jitkaew S, Cai Z. *et al.* Mixed lineage kinase domain-like is a key receptor interacting protein 3 downstream component of TNF-induced necrosis. *Proc Natl Acad Sci USA* 2012;**109**:5322–7.
70. Murphy JM, Czabotar PE, Hildebrand JM. *et al.* The pseudokinase MLKL mediates necroptosis via a molecular switch mechanism. *Immunity* 2013;**39**:443–53.

71. Bertheloot D, Latz E, Franklin BS. Necroptosis, pyroptosis and apoptosis: an intricate game of cell death. *Cell Mol Immunol* 2021;**18**:1106–21.
72. Cho YS, Challa S, Moquin D. *et al.* Phosphorylation-driven assembly of the RIP1-RIP3 complex regulates programmed necrosis and virus-induced inflammation. *Cell* 2009;**137**: 1112–23.
73. Li J, McQuade T, Siemer AB. *et al.* The RIP1/RIP3 necrosome forms a functional amyloid signaling complex required for programmed necrosis. *Cell* 2012;**150**:339–50.
74. Zhong Z, Liang S, Sanchez-Lopez E. *et al.* New mitochondrial DNA synthesis enables NLRP3 inflammasome activation. *Nature* 2018;**560**:198–203.
75. Liu Z, Wang M, Wang X. *et al.* XBP1 deficiency promotes hepatocyte pyroptosis by impairing mitophagy to activate mtDNA-cGAS-STING signaling in macrophages during acute liver injury. *Redox Biol* 2022;**52**:102305. https://doi.org/10.1016/j.redox.2022.102305.
76. Hopfner K-P, Hornung V. Molecular mechanisms and cellular functions of cGAS-STING signalling. *Nat Rev Mol Cell Biol* 2020;**21**:501–21.
77. Gaidt MM, Ebert TS, Chauhan D. *et al.* The DNA Inflammasome in Human Myeloid Cells Is Initiated by a STING-Cell Death Program Upstream of NLRP3. *Cell* 2017;**171**:1110–1124.e18.
78. Zhang X, Wu J, Liu Q. *et al.* mtDNA-STING pathway promotes necroptosis-dependent enterocyte injury in intestinal ischemia reperfusion. *Cell Death Dis* 2020;**11**:1050.
79. Brault M, Olsen TM, Martinez J. *et al.* Intracellular Nucleic Acid Sensing Triggers Necroptosis through Synergistic Type I IFN and TNF Signaling. *J Immunol*(Baltimore, Md. : 1950) 2018;**200**: 2748–56.
80. Zhang R, Kang R, Tang D. The STING1 network regulates autophagy and cell death. *Signal Transduction and Targeted Therapy* 2021;**6**:208.
81. Hwang I, Uchida H, Dai Z. *et al.* Cellular stress signaling activates type-I IFN response through FOXO3-regulated lamin posttranslational modification. *Nat Commun* 2021;**12**:640.
82. Orea-Soufi A, Paik J, Bragança J. *et al.* FOXO transcription factors as therapeutic targets in human diseases. *Trends Pharmacol Sci* 2022;**43**:1070–84.
83. Liu W, Li Y, Luo B. Current perspective on the regulation of FOXO4 and its role in disease progression. *Cellular and Molecular Life Sciences : CMLS* 2020;**77**:651–63.
84. Klotz L-O, Sánchez-Ramos C, Prieto-Arroyo I. *et al.* Redox regulation of FoxO transcription factors. *Redox Biol* 2015;**6**:51–72.
85. Manning BD, Cantley LC. AKT/PKB signaling: navigating downstream. *Cell* 2007;**129**:1261–74.
86. Ding Z, Dai C, Zhong L. *et al.* Neuregulin-1 converts reactive astrocytes toward oligodendrocyte lineage cells via upregulating the PI3K-AKT-mTOR pathway to repair spinal cord injury. *Biomedicine & Pharmacotherapy = Biomedecine & Pharmacotherapie* 2021;**134**:111168. https://doi.org/10.1016/j.biopha.2020.111168.
87. Bolino A, Piguet F, Alberizzi V. *et al.* Niacin-mediated Tace activation ameliorates CMT neuropathies with focal hypermyelination. *EMBO Molecular Medicine* 2016;**8**:1438–54.
88. Liu T, Zhang L, Joo D. *et al.* NF-kappaB signaling in inflammation. *Signal Transduct Target Ther* 2017;**2**:17023.